

New examination of the traditional Raman Lidar technique II: evaluating the ratios for water vapor and aerosols – Popular Summary

Submitted to Applied Optics

David N. Whiteman

This is the second of two papers providing a consistent, modern treatment of the analytical techniques required to derive meteorological quantities from Raman lidar measurements water vapor and aerosols. This new treatment is motivated by the rapid increase in the number of Raman lidar systems used around the world for these measurements and the lack of a thorough analytical treatment such as provided here. The topics covered here include the evaluation of the ratios of lidar measurements that lead to the meteorological quantities of water vapor mixing ratio, aerosol backscattering ratio and backscatter coefficient, and aerosol extinction to backscatter ratio. This treatment includes the effects of the temperature dependence of Raman scattering in all equations. The results indicate that current analytical techniques for the calculation of water vapor mixing ratio can be biased positive by 4-5% or more when using narrow spectral band detection. In addition, the calculation of aerosol backscatter coefficient, using the current techniques, can yield values that are biased low by more than 10%.

New examination of the traditional Raman Lidar technique II: evaluating the ratios for water vapor and aerosols

David N. Whiteman
NASA/Goddard Space Flight Center
Greenbelt, MD 20771

Abstract

In a companion paper, the temperature dependence of Raman scattering and its influence on the Raman and Rayleigh-Mie lidar equations was examined. New forms of the lidar equation were developed to account for this temperature sensitivity. Here those results are used to derive the temperature dependent forms of the equations for the water vapor mixing ratio, aerosol scattering ratio, aerosol backscatter coefficient, and extinction to backscatter ratio (S_a). The error equations are developed, the influence of differential transmission is studied and different laser sources are considered in the analysis. The results indicate that the temperature functions become significant when using narrowband detection. Errors of 5% and more can be introduced in the water vapor mixing ratio calculation at high altitudes and errors larger than 10% are possible for calculations of aerosol scattering ratio and thus aerosol backscatter coefficient and extinction to backscatter ratio. OCIS # 010.3640, 010.3920, 999.9999

1 Introduction

In part one of this paper [1] (hereafter referred to as "part I"), a detailed examination of how to evaluate the Raman and Rayleigh-Mie lidar equations was presented. The details considered there included the effects of the temperature sensitivity of Raman scattering in both the Raman and Rayleigh-Mie equations, the calculation of atmospheric transmission, multiple scattering effects and photon pulse pileup correction. This paper concerns evaluating the ratios that lead to the meteorological quantities of water vapor mixing ratio, aerosol scattering ratio and thus aerosol backscatter coefficient, and aerosol extinction/backscatter ratio.

The structure of the paper is as follows. First the temperature dependent forms of the Rayleigh-Mie and Raman lidar equations will be reviewed. Then the water vapor mixing ratio calculation is discussed. This includes an examination of the altitude dependence of the temperature functions, development of the error equations, examination of differential transmission and a discussion of calibration. The aerosol scattering ratio is then discussed along with the appropriate error equations and differential transmission is considered for different laser sources. The influence of narrowband detection on the calculations of aerosol backscattering coefficient are explored and then the extinction to backscatter ratio is covered.

1.1 The temperature dependent Rayleigh-Mie and Raman lidar equations

In part I [1], new forms of the lidar equation were derived that account for the influence of the temperature dependence of Raman rotational and vibrational-rotational scattering on the Rayleigh-Mie and Raman lidar equations. The final form of these equations will be repeated here for reference. Before proceeding, however, definitions given in part I will be reviewed for clarity. The term "Rayleigh scattering" will be used to signify the combination of Cabannes and

rotational Raman scattering [2] [3]. This recognizes the fact [2] [3] that what Lord Rayleigh [4] [5] actually detected was a combination of elastic and rotational Raman scattering. The term "Mie" scattering will be used to refer to scattering by particles of any shape even though the Mie theory [6] only pertains to spherical particles. Finally, the term "Rayleigh-Mie" lidar will be used to refer to systems that measure elastically scattered light from both molecules and particles of any shape as well as inelastically scattered pure rotational Raman scattering.

Now, the single-scattering Rayleigh-Mie and Raman lidar equations for the background-subtracted power received by a detector as a function of range can be expressed as follows

$$P(\Delta\lambda_R, r) = \frac{O_R(r) P_0(\lambda_L) A \xi(\lambda_L) \left(F_R(T) \beta_{\pi}^{mol}(\lambda_L, r) + \beta_{\pi}^{aer}(\lambda_L, r) \right)}{r^2} \times \exp\left(-2 \int_0^r \alpha(\lambda_L, r') dr'\right) \quad (1)$$

$$P(\Delta\lambda_X, r) = \frac{O_X(r) F_X(T) P_0(\lambda_L) A N_X(r) \frac{d\sigma_X(\pi)}{d\Omega} \xi(\lambda_X)}{r^2} \times \exp\left(-\int_0^r \{\alpha(\lambda_L, r') + \alpha(\lambda_X, r')\} dr'\right) \quad (2)$$

where $P(\lambda_R, r)$ is the backscattered power (after subtracting any background contribution due, for example, to sky-light or detector noise) received at the laser wavelength, λ_L , as a function of range, r . $O_R(r)$ is the Rayleigh-Mie channel overlap function, $P_0(\lambda_L)$ is the output power of the laser at the laser wavelength, λ_L . $\beta_{\pi}^{aer}(\lambda_L, r)$ is the backscatter coefficient at the laser wavelength and at range r due to Mie scattering. $\xi(\lambda_L)$ is the total lidar receiver optical efficiency at the laser wavelength and includes factors such as the reflectivity of the telescope, the transmission of conditioning optics, the transmission of any filters and the quantum efficiency of the detector. A is the receiver telescope area. The exponential factor gives the two-way atmospheric transmission, where $\alpha(\lambda_L, r)$ is the total extinction coefficient at the laser wavelength due to scattering and absorption by molecules, particles and any other atmospheric constituents such as water droplets or ice crystals as a function of range along the path of the laser beam.

$\beta_{\pi}^{mol}(\lambda_L, r) = N_R(r) d\sigma_R(\pi)/d\Omega$ and $d\sigma_R(\pi)/d\Omega$ is the full Rayleigh cross section including the effects of rotational Raman scattering. Notice that in the Rayleigh-Mie equation, the temperature dependent term $F_R(T)$ multiplies only $\beta_{\pi}^{mol}(\lambda_L, r)$ and not $\beta_{\pi}^{aer}(\lambda_L, r)$ since only the molecular component of the signal exhibits the temperature dependence considered here.

The terms used in the Raman lidar equation are defined similarly except that the atmospheric transmission term now involves both the outgoing wavelength of the laser and the return Raman shifted wavelength. Furthermore, in the Raman lidar equation there is no aerosol backscatter term so that the temperature dependent function multiplies the entire equation. This difference will become important in section 3 where the aerosol scattering ratio is considered.

The temperature dependent functions are defined by

$$F_X(T) = \frac{\int_{\Delta\lambda_X} \frac{d\sigma_X(\lambda', \pi, T)}{d\Omega} \xi(\lambda') d\lambda'}{\frac{d\sigma_X(\pi)}{d\Omega} \xi(\lambda_X)} \quad (3)$$

where X refers to either Rayleigh scattering (in which case rotational Raman lines carry the temperature dependence considered here) or for a Raman vibrational mode from molecular species X . $\xi(\lambda)$ is the lidar system transmission efficiency as a function of wavelength. The interval $\Delta\lambda_X$ is that over which the lidar system has significant transmission for feature X . $F_x(T) \frac{d\sigma_X(\pi)}{d\Omega}$ may be interpreted as the effective molecular cross section consistent with the use of a monochromatic optical efficiency term, $\xi(\lambda_X)$, in the lidar equation. These forms of the lidar equations will be used in the derivations to come after carefully considering the calculation of the transmission terms in the lidar equations.

2 Water vapor mixing ratio

2.1 Definition

Water vapor is one of the most important atmospheric state variables. The profile of water vapor in the atmosphere determines convective atmospheric stability which influences whether storm initiation is likely. It also is the most active greenhouse gas since it absorbs terrestrial radiation more strongly than CO_2 . The ratio of the mass of water

vapor and the mass of dry air in a given volume, known as the water vapor mixing ratio, is a convenient way to quantify the amount of water vapor in the atmosphere. The mixing ratio is conserved in atmospheric processes that do not involve condensation or evaporation and thus serves well as a tracer of the movement of air parcels in the atmosphere. The temperature dependent form of the water vapor mixing ratio equation will now be derived.

2.2 Calculation of the water vapor mixing ratio from the lidar equation

Using equation 2, the ratio of the single scattering Raman lidar measurements of water vapor and nitrogen, including the effects of temperature sensitivity, can be represented

$$\frac{P(\Delta\lambda_H, \tau)}{P(\Delta\lambda_N, \tau)} = \frac{O_H(r) F_H(T(r)) N_H(r) \frac{d\sigma_H(\pi)}{d\Omega} \xi(\lambda_H)}{O_N(r) F_N(T(r)) N_N(r) \frac{d\sigma_N(\pi)}{d\Omega} \xi(\lambda_N)} \Delta\tau(\lambda_H, \lambda_N, \tau) \quad (4)$$

where the shorthand notation

$$\Delta\tau(\lambda_H, \lambda_N, \tau) = \exp\left(-\int_0^\tau \{\alpha(\lambda_H, r') - \alpha(\lambda_N, r')\} dr'\right) \quad (5)$$

has been used for the differential transmission term, which accounts for the fact that atmospheric transmission differs at the two Raman wavelengths. Note the useful property that $\Delta\tau(\lambda_H, \lambda_N, \tau) = 1/\Delta\tau(\lambda_N, \lambda_H, \tau)$. Recalling that the water vapor mixing ratio is the ratio of the mass of water vapor and the mass of dry air, and considering that nitrogen forms a constant fraction (~ 0.78) of dry air in the lower atmosphere, it is apparent that

$$w = \frac{MW_{H_2O}}{MW_{DryAir}} \frac{N_H(r)}{N_{DryAir}(r)} \cong \frac{MW_{H_2O}}{MW_{DryAir}} \frac{N_H(r)}{N_N(r)/0.78} \cong 0.485 \frac{N_H(r)}{N_N(r)} \quad (6)$$

where w is the water vapor mixing ratio, MW_{H_2O} is the molecular weight of water vapor (18 g/mole), MW_{Air} is the molecular weight of dry air (an averaged quantity whose value is ~ 28.94 g/mole [7]). Combining equation 4 and 6 yields

$$w = k \frac{O_N(r) F_N(T) P(\lambda_H, r) \frac{d\sigma_N(\pi)}{d\Omega} \xi(\lambda_N)}{O_H(r) F_H(T) P(\lambda_N, r) \frac{d\sigma_H(\pi)}{d\Omega} \xi(\lambda_H)} \Delta\tau(\lambda_N, \lambda_H, r) \quad (7)$$

representing the constant of proportionality from equation 6 as $k (\cong 0.485)$.

For a perfect optical system, the ratio $O_N(r)/O_L(r)$ would be unity throughout the range of measurement. In a real lidar system, this ratio typically departs from unity for the ranges closest to the telescope. If this departure from unity is significant for the quantity being determined, the ratio of the overlap functions can be quantified by taking data in both channels using a common nitrogen or oxygen interference filter [8] [9] or by using more analytical techniques [10]. In the application of the common filter approach for quantifying the overlap function, care must be taken to use filters all of similar width since narrower filters are more subject to changes in transmission due to differing divergence angles that arise in the near-field [11]. In other words the common molecular filter should possess similar bandpass characteristics to the filters used for normal data acquisition. Furthermore, it is important to study the transmission and polarization characteristics of any intervening optics to insure that these properties do not change significantly between the nitrogen (or oxygen) wavelength used for determination of the overlap function and the wavelength of the species being measured in a given channel.

Another technique that can be used to reduce the influence of the overlap function is to acquire data at a small angle above the horizon, assume horizontal homogeneity over the atmosphere within a few kilometers of the lidar location, and convert the angle data to vertical data. This can limit the influence of the lidar overlap functions on the calculation of the water vapor mixing ratio to approximately the lowest 10-50 meters of the atmosphere [12]. Above this point, $O_N(r)/O_H(r)$ may then be considered constant and equal to unity. Using either of these approaches, above some point in the vertical profile, which can be as little as 10-50 m above the lidar site, the overlap functions no longer have an influence.

The water vapor mixing ratio equation can now be expressed using a single calibration factor as follows

$$w = k^*(r) \frac{F_N(T(r)) P(\lambda_H, r)}{F_H(T(r)) P(\lambda_N, r)} \Delta\tau(\lambda_N, \lambda_H, r) \quad (8)$$

$$k^*(r) \cong 0.485 \frac{O_N(r) \frac{d\sigma_N(\pi)}{d\Omega} \xi(\lambda_N)}{O_H(r) \frac{d\sigma_H(\pi)}{d\Omega} \xi(\lambda_H)} \quad (9)$$

where $k^*(r)$ is now the lidar system calibration factor. The temperature dependent ratio $F_N(T[r])/F_H(T[r])$,

which will be studied in the next section, now appears as a multiplier of the traditional Raman lidar water vapor mixing ratio equation [9] [13] [14].

The appropriate cross section values for different laser output wavelengths may be determined by using known values of cross section at 337.1 nm ($\text{cm}^2\text{sr}^{-1}$) [15] and accounting for the $(\nu - \Delta\nu)^4$ scaling of molecular scattering, where $\Delta\nu$ is the Raman frequency shift if present. Following this procedure for the XeF excimer laser (351.1 nm), tripled Nd:YAG laser (354.7 nm) and double Nd:YAG laser (532.07 nm) yields the following expressions for $k^*(r)$.

$$k_{351}^*(r) \cong 0.485 \frac{O_N(r) 2.9 \times 10^{-30} \xi(\lambda_N)}{O_H(r) 6.5 \times 10^{-30} \xi(\lambda_H)} \cong 0.22 \frac{O_N(r) \xi(\lambda_N)}{O_H(r) \xi(\lambda_H)} \quad (10)$$

$$k_{355}^*(r) \cong 0.485 \frac{O_N(r) 2.8 \times 10^{-30} \xi(\lambda_N)}{O_H(r) 6.2 \times 10^{-30} \xi(\lambda_H)} \cong 0.22 \frac{O_N(r) \xi(\lambda_N)}{O_H(r) \xi(\lambda_H)} \quad (11)$$

$$k_{532}^*(r) \cong 0.485 \frac{O_N(r) 4.6 \times 10^{-31} \xi(\lambda_N)}{O_H(r) 8.9 \times 10^{-31} \xi(\lambda_H)} \cong 0.25 \frac{O_N(r) \xi(\lambda_N)}{O_H(r) \xi(\lambda_H)} \quad (12)$$

The above expressions for the k^* factors demonstrate that the ratio of Raman cross sections is not constant due to the fact that $\Delta\nu$ is different for nitrogen and water vapor.

2.3 Temperature sensitivity functions versus altitude

The temperature sensitivity ratio $F_N(T(r))/F_H(T(r))$ that is needed to evaluate equation 8 is plotted versus altitude in figure 1 assuming the U. S. Standard Atmosphere temperature profile [16]. The following passbands were used for this illustration: water vapor - 18 and 120 cm^{-1} , nitrogen - 20 and 134 cm^{-1} . These correspond to ~0.3 and 2.0 nm passbands for 354.7 nm excitation as indicated in the legend. The 0.3 nm passband approximates that of such systems as the Department of Energy's Raman Lidar [17] and the NASA/GSFC Scanning Raman Lidar in its daytime measurement configuration [18]. The other temperature sensitivity functions $F_R(r)$, $F_O(r)$, $F_N(r)$ are needed for the calculation of the aerosol scattering ratio, which will be covered later. They are also displayed using passband widths that correspond to 0.3 and 2.0 nm when using 354.7 excitation.

It is interesting to note that for the case of the ratio $F_N(T(r))/F_H(T(r))$ pertinent to the calculation of water vapor mixing ratio, the use of narrow passband (0.3 nm when excited at 354.7 nm) for both water vapor and nitrogen

channels yields a temperature sensitivity ratio that decreases approximately 4% between the surface and 11 km while the use of wide passband (2.0 nm) for both channels yields a ratio that increases approximately 0.6% over the same range. Other combinations of passband widths and positions can increase this effect to much larger than 5% [1]. It is clear from this figure that certain combinations of passband center and width for the two channels can be found that yield an altitude independent ratio. For example the combination of approximately 55 cm^{-1} passband for both water vapor and nitrogen would yield a ratio of $F_N(T(r))/F_H(T(r))$ that is independent of height [1]. The error equations for the mixing ratio will now be formulated.

2.4 Water vapor mixing ratio error equations

The random error in determining w is given by applying standard error propagation formulas [19] to equation 8. The result, which has been presented before [20] but will be repeated here for completeness, is

$$\frac{\sigma_w^2}{w^2} = \frac{\sigma_{k^*}^2}{k^{*2}} + \frac{\sigma_{R_w}^2}{R_w^2} + \frac{\sigma_{\Delta\tau}^2}{\Delta\tau^2} \quad (13)$$

where the abbreviation $R_w = P(\lambda_H, r)/P(\lambda_N, r)$ has been used. The full quantification of equation 13 requires analysis of the variation of all random factors that go into the calibration of the water vapor mixing ratio. The Raman lidar calibration has been shown to be very stable over periods of years [21] [14] when system components are not changed thus the variance in k^* can be considered to be very small. Errors introduced by uncertainties in the water vapor mixing ratio differential transmission term will be studied in the next section where it will be shown that, by using the Raman lidar measurement of aerosol extinction in addition to molecular number density obtained from radiosonde, error in this term can be kept very small also. Thus the random error in the ratio of the lidar signals usually dominates the error budget. These errors will now be quantified using Poisson statistics.

Recalling that the P terms in equation 8 are actually background subtracted quantities, $\sigma_{R_w}^2/R_w^2$ may be expressed using the following substitutions $P(\lambda_H, r) = S_H - B_H$ and $P(\lambda_N, r) = S_N - B_N$ where S refers to the laser induced signals and B refers to the background terms as follows

$$\frac{\sigma_{R_w}^2}{R_w^2} = \frac{\sigma_{S_H}^2 + \sigma_{B_H}^2}{(S_H - B_H)^2} + \frac{\sigma_{S_N}^2 + \sigma_{B_N}^2}{(S_N - B_N)^2} \quad (14)$$

$$\sigma_{R_w}^2 = \frac{(S_H - B_H)^2}{(S_N - B_N)^2} \left(\frac{\sigma_{S_H}^2 + \sigma_{B_H}^2}{(S_H - B_H)^2} + \frac{\sigma_{S_N}^2 + \sigma_{B_N}^2}{(S_N - B_N)^2} \right) \quad (15)$$

where it is explicitly shown that there is error in the determination of the backgrounds. Under certain conditions, such as high background during daytime measurements, these error sources can become significant.

2.5 Water vapor mixing ratio differential transmission

The differential transmission (DT) term $\Delta\tau(\lambda_N, \lambda_H, \tau)$ in equation 28, which accounts for the fact that the return signals at λ_N and λ_H experience different attenuations on their return trips from the scattering volume, will now be computed. The influence of various aerosol loadings on this calculation will be studied using several synthesized aerosol extinction profiles.

The synthesized profiles are shown in figure 2 where each of the profiles equals zero above an altitude of 2 km. These aerosol extinction profiles, along with the molecular extinction calculated using the techniques outlined in part I using the molecular number density values from the U.S. Standard Atmosphere [16], were used to calculate the water vapor DT profiles shown in figure 3. The profiles can be considered appropriate for water vapor mixing ratio measurements made with either the XeF excimer (351.1 nm) or tripled Nd:YAG (355 nm) laser since the differential transmission values differ by less than 1%. The aerosol optical depth, considered to be at the laser wavelength, for each of these profiles is obtained by integrating the extinction from 0 - 2 km. The aerosol optical depths, τ , that result are shown in the legend of the figure. They range from a pure Rayleigh atmosphere ($\tau = 0$) to an extremely hazy value of $\tau = 2.0$. In these plots, a range independent Angstrom coefficient of $k = 1.0$ was used.

For a pure Rayleigh atmosphere, the value of the water vapor DT varies from 1 at the surface to approximately 0.92 at 20 km. For an aerosol optical depth of 0.5 the range of values increases to 1.0 - 0.90. As aerosol loading increases, the DT values becomes smaller. Notice that the curves are all parallel above 2 km. This figure shows the importance, particularly under hazy conditions, of having a simultaneous measurement of aerosol extinction for the calculation of

differential transmission.

Since the Raman lidar can be used to measure the round-trip aerosol extinction directly, actual lidar profiles of aerosol extinction can be used to generate the required differential transmission term. However, there still remains the uncertainty in what value of $k(r)$ to use in the calculation of the one-way aerosol extinction since variations in k influence the Raman derived extinction [12] [1]. Additional aerosol information such as provided by a sun photometer, although limited to total column averages, can be useful in this analysis. To test the sensitivity of the differential transmission to changes in the Angstrom coefficient, k , for an upward looking system with output wavelength of 351 nm, figure 4 was generated using various values of k for an aerosol optical depth of 1.0. Varying k from 0.8 to 1.2 causes only a 2% change in the differential transmission. The relatively low sensitivity of the differential transmission to variations in k implies that variations in $k(r)$ within the column will have a small influence on the profile of differential transmission under most circumstances.

The doubled Nd:YAG laser (~532 nm) is a less popular choice for making water vapor mixing ratio measurements than UV lasers such as the tripled Nd:YAG (~355 nm) for several reasons including the reduced Raman scattering cross section, lower efficiency of detectors for use at the water vapor shifted wavelength of ~660 nm and the fact that water vapor absorbs weakly at 660 nm but not at 607 nm. This difference in absorption between 607 nm and 660 nm implies that the calculation of the differential transmission that is needed in equation 8 must account for both scattering and absorption. A radiative transfer model such as Modtran [22] can be used for this calculation. The DT profiles will differ from the ones calculated based on pure molecular scattering by up to ~1% based on Modtran calculations using the standard tropical atmosphere [16]. The effect of the absorption of the water vapor wavelength is to decrease the amount of differential transmission experienced by the two return signals. To obtain the DT profile with the highest accuracy would require an iteration due to the fact that, in the Raman lidar equation, water vapor is responsible for both backscatter and extinction.

2.6 Raman lidar water vapor mixing ratio calibration

The issue of lidar calibration is a very important one since this is the process that leads to useful meteorological

quantities. There are different approaches that have been taken in the effort to calibrate the water vapor measurements of a Raman lidar system. Among them are 1) by an atmospheric calibration assuming saturation at cloud base [23], 2) by comparison with another water vapor sensor such as a radiosonde [21] or microwave radiometer [14], and 3) by a first principles calibration that accounts for the total efficiency of transmitting photons through the atmosphere, scattering them off of the molecules of interest and then detecting them with the lidar receiver system [24].

2.7 Calibration with respect to other water vapor sensors and at the base of clouds

The NASA/GSFC Scanning Raman Lidar (SRL) was stationed on Andros Island, Bahamas during July - September, 1998 for the third Convection and Moisture (CAMEX-3) hurricane study program [23]. At the time of that deployment, the SRL used a XeF excimer laser (351 nm), 0.76 m telescope and high and low range photomultiplier tubes to measure each of the Rayleigh-Mie, oxygen, nitrogen and water vapor signals [18]. The passbands of the water vapor and nitrogen channels were 8.6 nm and 8.0 nm, respectively. It is important to note that use of such wide spectral passbands essentially eliminates the issues relating to temperature sensitivity studied here [25].

The final SRL water vapor mixing ratio calibration constant for the CAMEX-3 campaign was derived in two ways that resulted in nearly identical values. One was through the use of 31 Vaisala radiosonde comparisons, where the radiosondes were corrected for the known dry bias in the sondes [26] [27]. The other technique was based on a set of lidar water vapor and radiosonde temperature measurements made at the base of marine boundary layer cumulus clouds assuming that saturation obtained at cloud base [23]. The mean calibration constant derived using these two techniques differed by less than 1% indicating that, at least for the CAMEX-3 campaign, the Vaisala dry bias correction performed well. The standard deviation of the cloud base derived calibration constant was 3% while that of the radiosonde derived calibration constant was 5% indicating that the cloud base technique was a more stable calibration source than the radiosonde.

An example of a lidar/radiosonde comparison is shown in figure 5 using data acquired over a 10-minute period on August 22, 1998 at Andros Island during CAMEX-3. The calibration constant, k^* , from equation 10 and determined using the cloud base calibration technique was ~ 0.204 . Using this value of k^* in equation 8 produces the lidar water

vapor mixing ratio in units of kg of water vapor per kg of dry air. The units of mixing ratio typically used in these plots, however, are grams of water vapor per kilogram of dry air (g/kg) which is obtained by multiplying by 1000. It is interesting to note that the calibration value of 0.204 indicates that, using equation 10, the ratio of lidar system efficiencies, $\xi(\lambda_N)/\xi(\lambda_H) = 0.204/0.22 \cong 0.93$. In other words, the SRL optical detection system has $\sim 7\%$ higher efficiency in the water vapor channel than in the nitrogen channel. This was the result of an optical design which maximized the transmission of the water vapor wavelength at the expense of the other (stronger) signals such as nitrogen.

The data are shown in the figure both on a linear scale on the left and on a log scale on the right. The linear scale shows the discrepancy between the lidar and the radiosonde in the first kilometer with the radiosonde showing a low-level moisture inversion. This may be a real event in the atmosphere or it could also be an indication that the radiosonde required some time to equilibrate to the environment [28]. The log scale on the right shows the good agreement of the two sensors in the upper regions of the profile where mixing ratio values approach $0.1 g/kg$. The lidar data on the left are plotted with $75 m$ vertical resolution. The lidar data on the right use $75 m$ resolution up to $6 km$, $225 m$ resolution between $6 - 8 km$ and $375 m$ above $8 km$. In general the random error increases with height reaching approximately 20% at $10km$.

Another method of calibration is that used by the DOE CART Raman lidar, which is calibrated by comparing the total precipitable water of the lidar profile to that of a collocated microwave radiometer [14]. The calibration constant derived using this technique has proven to be very stable. Between August, 1998 and January, 2000 the standard deviation of the CARL calibration constant was 3% while the standard error of this constant was 0.04% [29] demonstrating that, if no changes are made to a Raman water vapor lidar system, stable long term calibration is possible.

2.8 First principles Raman water vapor lidar calibration

Examination of equation 8 indicates that a first principles Raman water vapor lidar calibration requires the ratio of transmissions of the lidar water vapor and nitrogen channels, the ratio of Raman scattering cross sections from nitrogen

(or oxygen) and water vapor, the temperature dependent functions and the differential transmission. Preceding sections have dealt with how to determine the latter two quantities with accuracies ~1-2%. To pursue an absolute calibration, the ratio of lidar channel transmissions and the ratio of Raman cross sections must be quantified with accuracy as well.

The efficiency ratio $\xi(\lambda_N)/\xi(\lambda_H)$ can be determined with high accuracy through the use of a black body calibration lamp. For example, UV calibration lamps that are traceable to the National Institutes of Standards and Technology with 2% accuracy are easily available. The 2% uncertainty in the intensity of the lamp source is due to the uncertainty in the effective color temperature of the lamp, which for a 2% error in intensity is ~5K. However, it is the ratio of intensities at λ_N and λ_H that is needed for the Raman lidar calibration and a lamp with 2% absolute accuracy can be used to quantify the ratio of intensities at two closely spaced wavelengths such as λ_N and λ_H to within ~0.1%. Therefore a highly accurate calibration source is available for quantifying $\xi(\lambda_N)/\xi(\lambda_H)$.

The knowledge of the ratio of cross sections $\frac{d\sigma_N(\pi)}{d\Omega}/\frac{d\sigma_H(\pi)}{d\Omega}$ is limited by the fact that the best available laboratory measurements of the water vapor cross section date from 1976 and have an uncertainty of $\pm 10\%$ [30]. Therefore any absolute calibration effort that relies on the currently available cross sections for nitrogen and water vapor will have a total error that exceeds 10%. The first documented effort to perform an absolute Raman water vapor calibration was by Vaughan et. al. [8]. Their effort resulted in an error estimate of 12% while the more recent effort of Sherlock et. al. [24] estimated a total error of 12-14%. The largest uncertainty in both of these efforts was the knowledge of the cross section ratio for nitrogen and water vapor and nitrogen.

The relative line strengths in the Raman spectra from water vapor [31], nitrogen and oxygen [32] [33] [34] can now be modeled with high precision. This ability coupled with an accurate measurement of $\xi(\lambda_N)/\xi(\lambda_H)$ for the lidar system and an accurate calibration with respect to another sensor could potentially be used to improve the knowledge of the ratio of water vapor and nitrogen cross sections. For example, the standard error of the CARL calibration constant with respect to the DOE/ARM microwave radiometer, which is believed to possess an absolute water vapor accuracy of better than 4% for precipitable water amounts in excess of 1 cm [35], is 0.04%. In other words the CART Raman lidar calibration is very stable and well determined. That coupled with the high relative accuracy in the line strengths of the Raman water vapor and nitrogen spectra available through modeling imply that stable, long-term measurements

of the lidar calibration constant such as those of the CART Raman lidar, when coupled with radiometric measurements of the optical transmission efficiency, could be used to improve the knowledge of the atmospheric cross section ratio $\frac{d\sigma_N(\pi)}{d\Omega} / \frac{d\sigma_H(\pi)}{d\Omega}$. A measurement of the cross section ratio with ~4-5% accuracy appears possible. Therefore it seems feasible that an absolute Raman water vapor lidar calibration could be performed in the future with total error of perhaps 5-7% using this approach.

3 Aerosol scattering ratio

3.1 Definitions

The aerosol scattering ratio is used to quantify the ratio of aerosol (or Mie scattering) and molecular scattering. It is defined as the ratio of the volume backscatter coefficients for total (molecular + aerosol) scattering and pure molecular scattering and can be expressed as

$$\mathcal{R}(\lambda_L, r) = \frac{\beta_{\pi}^{\text{tot}}(\lambda_L, r)}{\beta_{\pi}^{\text{mol}}(\lambda_L, r)} = \frac{\beta_{\pi}^{\text{mol}}(\lambda_L, r) + \beta_{\pi}^{\text{aer}}(\lambda_L, r)}{\beta_{\pi}^{\text{mol}}(\lambda_L, r)} = 1 + \frac{\beta_{\pi}^{\text{aer}}(\lambda_L, r)}{\beta_{\pi}^{\text{mol}}(\lambda_L, r)} \quad (16)$$

where the volume backscatter coefficient for molecules $\beta_{\pi}^{\text{mol}}(\lambda_L, r)$ is given by $N^{\text{mol}}(r) d\sigma_{\text{mol}}(\pi) / d\Omega$ [1].

3.2 Formulation of the equations for aerosol scattering ratio

The Raman lidar is able to quantify the aerosol scattering ratio in a more direct manner than elastic lidar systems. The Raman lidar measures a signal proportional to the molecular nitrogen (or oxygen) density. This can be used as a direct quantification of the denominator needed in equation 16. A simple elastic lidar has no such signal and must resort to inversions to determine this ratio.

The calculation of the aerosol scattering ratio from the basic Raman lidar signals will now be described. Forming the ratio of equations 1 and 2 for the background-subtracted lidar received power at the laser wavelength, λ_L , and at the Raman nitrogen wavelength, λ_N , yields

$$\begin{aligned}
\frac{P(\Delta\lambda_R, r)}{P(\Delta\lambda_N, r)} &= \frac{O_R(r) \xi(\lambda_L)}{O_N(r) \xi(\lambda_N)} \frac{F_R(T(r))\beta_\pi^{mol}(\lambda_L, r) + \beta_\pi^{aer}(\lambda_L, r)}{F_N(T(r))N_N(r) \frac{d\sigma_N(\pi)}{d\Omega}} \exp\left(-\int_0^r \{\alpha(\lambda_L, r') - \alpha(\lambda_N, r')\} dr'\right) \\
&= \frac{O_R(r) \xi(\lambda_L)}{O_N(r) \xi(\lambda_N)} \frac{F_R(T(r))\beta_\pi^{mol}(\lambda_L, r) + \beta_\pi^{aer}(\lambda_L, r)}{F_N(T(r))N_N(r) \frac{d\sigma_N(\pi)}{d\Omega}} \Delta\tau(\lambda_L, \lambda_N, r) \quad (18)
\end{aligned}$$

The Raman backscatter coefficient for nitrogen molecules is $\beta_\pi^N(\lambda_L, r) = N_N(r) d\sigma_N(\pi)/d\Omega$ and is proportional to the Rayleigh backscattering coefficient for air since nitrogen is well mixed in the lower atmosphere. This fact can be expressed as

$$\beta_\pi^N(\lambda_L, r) = C_N \beta_\pi^{mol}(\lambda_L, r) \quad (19)$$

If the Raman oxygen signal is used to normalize the scattering ratio then the following equation pertains.

$$\beta_\pi^O(\lambda_L, r) = C_O \beta_\pi^{mol}(\lambda_L, r) \quad (20)$$

The proportionality factor C_N in equation 19 can be calculated for the use of different laser sources by scaling cross section values from 337.1 nm [15] and by noting that nitrogen and oxygen form ~0.78 and ~0.21 of the atmosphere as follows:

$$C_N(\lambda_L = 351) \cong \frac{1}{0.78} \frac{\beta_\pi^N(\lambda_L = 351, r)}{\beta_\pi^{mol}(\lambda_L = 351, r)} \cong \frac{1}{0.78} \frac{2.9 \times 10^{-30}}{3.3 \times 10^{-27}} \cong 1.1 \times 10^{-3} \quad (21)$$

$$C_N(\lambda_L = 355) \cong \frac{1}{0.78} \frac{\beta_\pi^N(\lambda_L = 355, r)}{\beta_\pi^{mol}(\lambda_L = 355, r)} \cong \frac{1}{0.78} \frac{2.8 \times 10^{-30}}{3.2 \times 10^{-27}} \cong 1.1 \times 10^{-3} \quad (22)$$

$$C_N(\lambda_L = 532) \cong \frac{1}{0.78} \frac{\beta_\pi^N(\lambda_L = 532, r)}{\beta_\pi^{mol}(\lambda_L = 532, r)} \cong \frac{1}{0.78} \frac{4.6 \times 10^{-31}}{6.3 \times 10^{-28}} \cong 9.4 \times 10^{-4} \quad (23)$$

The appropriate constants for use of oxygen in normalizing the scattering ratio are:

$$C_O(\lambda_L = 351) \cong \frac{1}{0.21} \frac{\beta_\pi^O(\lambda_L = 351, r)}{\beta_\pi^{mol}(\lambda_L = 351, r)} \cong \frac{1}{0.21} \frac{3.9 \times 10^{-30}}{3.3 \times 10^{-27}} \cong 5.6 \times 10^{-3} \quad (24)$$

$$C_O(\lambda_L = 355) \cong \frac{1}{0.21} \frac{\beta_\pi^O(\lambda_L = 355, r)}{\beta_\pi^{mol}(\lambda_L = 355, r)} \cong \frac{1}{0.21} \frac{3.7 \times 10^{-30}}{3.2 \times 10^{-27}} \cong 5.6 \times 10^{-3} \quad (25)$$

$$C_O(\lambda_L = 532) \cong \frac{1}{0.21} \frac{\beta_\pi^O(\lambda_L = 532, r)}{\beta_\pi^{mol}(\lambda_L = 532, r)} \cong \frac{1}{0.21} \frac{6.5 \times 10^{-31}}{6.3 \times 10^{-28}} \cong 4.9 \times 10^{-3} \quad (26)$$

Equation 18 and 19 can now be combined to yield an expression for $\mathcal{R}(\lambda_L, r)$. The result is

$$\mathcal{R}(\lambda_L, r) - 1 = \frac{\beta_{\pi}^{aer}(\lambda_L, r)}{\beta_{\pi}^{mol}(\lambda_L, r)} = C_N(\lambda_L) F_N(T(r)) \frac{O_N(r) \xi(\lambda_N) P(\Delta\lambda_R, r)}{O_R(r) \xi(\lambda_L) P(\Delta\lambda_N, r)} \Delta\tau(\lambda_N, \lambda_L, r) - F_R(T(r)) \quad (27)$$

A similar expression can be derived for the use of oxygen as the normalizing signal in the scattering ratio. Absorbing the overlap and efficiencies from equation 27 into a new term, $C_N^*(\lambda_L, r)$, yields

$$\mathcal{R}(\lambda_L, r) - 1 = C_N^*(\lambda_L, r) F_N(T(r)) \frac{P(\Delta\lambda_L, r)}{P(\Delta\lambda_N, r)} \Delta\tau(\lambda_N, \lambda_L, r) - F_R(T(r)) \quad (28)$$

$$C_N^*(\lambda_L, r) = C_N(\lambda_L) \frac{O_N(r) \xi(\lambda_N)}{O_R(r) \xi(\lambda_L)} \quad (29)$$

Due to the fact that in equation 18 $F_R(T(r))$ multiplies only $\beta_{\pi}^{mol}(\lambda_L, r)$ and not $\beta_{\pi}^{aer}(\lambda_L, r)$, the result achieved in 28 for the aerosol scattering ratio is not simply a temperature dependent factor times the traditional result [9] [13] [12] [14] as it was for the water vapor mixing ratio. The effect of the temperature dependent functions in equation 28 will be covered in section 3.5, which concerns atmospheric calibration of the aerosol scattering ratio.

3.2.1 Temperature sensitivity factors for the scattering ratio calculation

The temperature sensitivity functions, $F_R(r)$, $F_O(r)$ and $F_N(r)$ needed for evaluating 28 were shown in figure 1. $F_O(r)$ was included in the figure since the Raman signal from molecular oxygen can be used equally well in forming the aerosol scattering ratio. There is an advantage in doing so when it comes to calculating the differential transmission function as will be shown shortly. In general, $F_X(r) \frac{d\sigma_X(\pi)}{d\Omega}$ quantifies the effective molecular cross section consistent with the use of a monochromatic optical efficiency term $\xi(\lambda_X)$ in the lidar equation. A narrower bandpass transmits less of the rotational (or vibrational-rotational) Raman lines and thus less of the total cross section. In the case of O_2 , the fraction of total cross section that is present in the vibrational-rotational lines is larger than for N_2 as shown in figure 1. Thus, for comparable bandpass widths, $F_O(r)$ has a smaller value than $F_N(r)$. The evaluation of the calibration constant $C_{N,O}^*(\lambda_L, r)$ and the differential transmission term will be discussed after the error equations are developed.

3.3 Aerosol scattering ratio error equations

The random component of the error in determining $\mathcal{R}(\lambda_L, r)$ is given by applying standard error propagation formulas [19] to equation 28. The result is

$$\frac{\sigma_{\mathcal{R}}^2}{\mathcal{R}^2} = \frac{\sigma_{C_N^*}^2}{C_N^{*2}} + \frac{\sigma_A^2}{A^2} + \frac{\sigma_{\Delta\tau}^2}{\Delta\tau^2} \quad (30)$$

$$\sigma_{\mathcal{R}}^2 = T^2 \left(\frac{\sigma_{C_N^*}^2}{C_N^{*2}} + \frac{\sigma_{F_N}^2}{F_N^2} + \frac{\sigma_A^2}{A^2} + \frac{\sigma_{\Delta\tau}^2}{\Delta\tau^2} \right) + \sigma_{F_R}^2 \quad (31)$$

where the following shorthand notation has been used

$$T = C_N^*(\lambda_L, r) F_N(T(r)) A \Delta\tau(\lambda_N, \lambda_L, r) \quad (32)$$

$$A = \frac{P(\Delta\lambda_R, r)}{P(\Delta\lambda_N, r)} \quad (33)$$

where A represents the ratio of the background subtracted lidar signals, $P(\Delta\lambda_R, r)/P(\Delta\lambda_N, r)$, in equation 28. Variations in the calibration factor, $C_N^*(\lambda_L, r)$, and the differential transmission, $\Delta\tau$, will be studied in the next sections. It will be shown that the atmosphere offers a natural calibration tool that permits accurate scattering ratio calibrations. Furthermore, errors in the differential transmission term can be kept small through a direct measurement of aerosol extinction. Quantifying the error in the knowledge of the temperature sensitivity functions $F_N(T)$ (or $F_O(T)$) and $F_R(T)$ is rather complex since the error is related to the uncertainty in the passband shape, the atmospheric temperature and the spectrum of the molecular feature being measured. However, the overall effect of both of these temperature dependent functions on the calculation of scattering ratio is on the order of 10%. The uncertainty in the calculation of the temperature dependent functions can be made less than 10% implying that the contribution of the temperature dependence to the error budget can be kept below 1%. Therefore, the random error in the calculation of scattering ratio is typically dominated by the uncertainty in the lidar signals themselves. Therefore, quantifying the standard error in the aerosol scattering ratio as being determined by the random error in the lidar signals is a good approximation. The equations are:

$$\frac{\sigma_{\mathcal{R}}^2}{\mathcal{R}^2} \cong \frac{\sigma_{SL}^2 + \sigma_{BL}^2}{(S_L - B_L)^2} + \frac{\sigma_{SN}^2 + \sigma_{BN}^2}{(S_N - B_N)^2} \quad (34)$$

$$\sigma_{\mathcal{R}}^2 \cong \frac{(S_L - B_L)^2}{(S_N - B_N)^2} \left(\frac{\sigma_{SL}^2 + \sigma_{BL}^2}{(S_L - B_L)^2} + \frac{\sigma_{SN}^2 + \sigma_{BN}^2}{(S_N - B_N)^2} \right) \quad (35)$$

where the subscripts L and N refer to the signals at the laser wavelength and the Raman-shifted nitrogen wavelength. A point to note here is that the errors in the determination of the backgrounds, σ_{BL}^2 and σ_{BN}^2 , propagate into the total error in the aerosol scattering ratio calculation in the same way as for the water vapor mixing ratio calculation.

3.4 Aerosol scattering ratio differential transmission

The differential transmission term $\Delta\tau(\lambda_N, \lambda_L, r)$ in equation 28, which accounts for the fact that the return signals at λ_L and λ_N experience different attenuations on their return trips from the scattering volume, will now be computed. The influence of various aerosol loadings on this calculation will be studied using the same synthesized aerosol extinction profiles shown in figure 2 that were used for the calculation of water vapor differential transmission.

The differential transmission functions that results from using these aerosol extinction profiles and molecular extinction calculated using the U.S. Standard Atmosphere density profile [16] are shown in figure 6 for the use of the XeF excimer laser (351 nm). The differential transmission function pertaining to the use of the Raman nitrogen signal in the calculation of aerosol scattering ratio is shown on the left and that for oxygen is shown on the right. As stated earlier, the use of the oxygen signal in the scattering ratio calculation has an advantage because the differential transmission is smaller.

For a moderately turbid value of aerosol optical depth of 0.5 (at 351 nm), the differential transmission term changes by less than 5% at 20 km from the pure Rayleigh value for the use of either the nitrogen or oxygen signal. However, under the extremely hazy conditions of an aerosol optical depth of 2.0, the value of the differential transmission term increases to approximately 1.4 (1.25) at 20 km from its pure Rayleigh value of approximately 1.15 (1.12) when using the Raman nitrogen (oxygen) signal in the scattering ratio calculation. The differential transmission curves are essentially parallel to each other above 2 km, as in the case of the water vapor calculation shown earlier, since the

aerosols are confined to a region below 2 *km* in the synthetic profiles.

The value chosen for the Angstrom coefficient influences the calculation of the differential transmission term as shown in figure 7. Varying the Angstrom coefficient over a range of 0.8 to 1.2 for the case of aerosol optical depth of 1.0 causes a 4% change in the differential transmission term needed when using the Raman nitrogen signal in the scattering ratio calculation. Thus, under very hazy conditions, a knowledge of the wavelength scaling of the aerosols present, such as can be obtained by sun photometer, can help to reduce the uncertainty in this term. (However, a sun photometer only yields the column average Angstrom coefficient. A multi-wavelength lidar [36] [37] can be used to quantify the Angstrom coefficient as a function of range but that is beyond the scope of the present treatment, which is confined to a single output laser wavelength.)

The differential transmission profiles for use with the doubled (~355 nm) and tripled (~532 nm) Nd:YAG are shown in figure 8 for use of both nitrogen (left) and oxygen (right) in the denominator. Three scenarios are considered: 1) pure Rayleigh atmosphere, 2) aerosol optical depth of 1.0 at both 355 nm and 532 nm and 3) aerosol optical depth of 1.0 at 355 nm and 0.67 at 532 nm. This latter case is provided as a more realistic comparison of the DT profile for the two laser sources operated under the same atmospheric conditions. The advantage of the oxygen signal for the aerosol scattering ratio is again clear. As a general statement, the differential transmission when using oxygen in the denominator is approximately 60% of the value when using nitrogen. For either the oxygen or nitrogen case, the DT for a pure Rayleigh atmosphere is much less for the doubled Nd:YAG (532) than for the tripled Nd:YAG ("less differential transmission" is used to mean that the values are closer to 1.0). When aerosol loading is considered, the differential transmission within the aerosol regions is more similar between the two output wavelengths than it is in the aerosol-free atmosphere. For the $\tau = 1.0$ case, with either oxygen or nitrogen in the denominator, the differential transmission within the first 2 km is actually larger for the 532nm output than the 355nm output. This is due to the larger wavelength separation of the Rayleigh-Mie and nitrogen (or oxygen) wavelengths when excited at 532 nm than at 355 nm and the assumption in these plots that aerosol scattering scales as λ^{-1} while molecular scattering scales approximately as λ^{-4} . However, a value of aerosol optical depth of 0.67 at 532 nm is consistent with an aerosol optical thickness (AOT) of 1.0 at 355 nm and an Angstrom coefficient of 1.0. The use of this AOT yields slightly

smaller DT values than the $\tau(355nm) = 1.0$ case.

3.5 Atmospheric calibration of the aerosol scattering ratio

The atmosphere offers a natural calibration tool for determining the factor $C_{N,O}^*(\lambda_L, \tau)$ in equation 28. In non-volcanic conditions and in the absence of desert dust, Russell et. al. [38] [39] demonstrate that, except for clouds, there are very few aerosols present in the free troposphere (above the boundary layer but below the tropopause). They show that the minimum value of aerosol scattering ratio $\mathcal{R}_{min}(\lambda)$ for a wavelength of 690 nm is not greater than 1.02. Using this value of $\mathcal{R}_{min}(\lambda)$ and a λ^{-4} dependence for Rayleigh scattering and assuming a λ^{-k} dependence in aerosol scattering coefficient (considered constant as a function of range) implies that the correct value of $\mathcal{R}_{min}(\lambda)$ can be determined in the following manner.

The wavelength scaling of the Rayleigh and Mie backscattering coefficients may be expressed as

$$\frac{\beta_{\pi}^{mol}(\lambda_1, r)}{\beta_{\pi}^{mol}(\lambda_2, r)} = \left(\frac{\lambda_2}{\lambda_1}\right)^4 \quad (36)$$

$$\frac{\beta_{\pi}^{aer}(\lambda_1, r)}{\beta_{\pi}^{aer}(\lambda_2, r)} = \left(\frac{\lambda_2}{\lambda_1}\right)^k \quad (37)$$

Given that the aerosol scattering ratio at wavelength λ_1 is

$$\mathcal{R}(\lambda_1, r) = 1 + \frac{\beta_{\pi}^{aer}(\lambda_1, r)}{\beta_{\pi}^{mol}(\lambda_1, r)} \quad (38)$$

equations 36 and 37 can now be used in conjunction with equation 16, the expression for aerosol scattering ratio, to scale the scattering ratio to different wavelengths. Therefore, at λ_2 the following equation pertains

$$\mathcal{R}(\lambda_2, r) = 1 + \frac{(\lambda_1/\lambda_2)^k \beta_{\pi}^{aer}(\lambda_1, r)}{(\lambda_1/\lambda_2)^4 \beta_{\pi}^{mol}(\lambda_1, r)} = 1 + \frac{\beta_{\pi}^{aer}(\lambda_1, r)}{(\lambda_1/\lambda_2)^{4-k} \beta_{\pi}^{mol}(\lambda_1, r)} \quad (39)$$

Using now the values of $\lambda_1 = 690 \text{ nm}$, $\lambda_2 \cong 350 \text{ nm}$, $\mathcal{R}_{min}(690, r) = 1.02$, and $k = 1$ yields $\mathcal{R}_{min}(350, r) \cong 1.003$. The Angstrom coefficient, k , generally varies between the extremes of approximately 0 and 2. Even assuming the maximum value of $k = 2$, $\mathcal{R}_{min}(350, r) \cong 1.005$. Due to the very small value of $\mathcal{R}_{min}(\lambda = 350, r)$ for

all values of k , the calibration of the aerosol backscattering ratio can be performed by assuming that the minimum value of backscattering ratio that a UV Raman lidar measures between 6 and 10 km corresponds to an aerosol backscattering ratio of 1.0. The error in this assumption is much less than 1%. For a visible Raman lidar operating at 532 nm, however, the appropriate normalization value $\mathcal{R}_{min}(532, r) \cong 1.01$.

Although the atmosphere offers a convenient calibration source for the aerosol scattering ratio calculation, the inclusion of the temperature sensitive functions in equation 28 changes this calculation significantly from what has traditionally been done using Raman lidar [9] [13]. This will now be discussed.

3.5.1 The effect of the temperature sensitivity functions

After applying the differential transmission functions as shown above and accounting for $F_N(T)$ (or $F_O(T)$) and $F_R(T)$ in equation 28, $C_N^*(\lambda_L, r)$ is chosen such that $C_N^*(\lambda_L, r) F_N(T(r)) P(\lambda_L, r) / P(\lambda_N, r) \Delta\tau(\lambda_N, \lambda_L, r) - F_R(T(r)) = 1.0$ in a region of the atmosphere which is free of aerosols. $F_N(T(r))$ is a multiplicative factor implying that only changes in the value of F_N between the reference point (typically ~ 8 km) and where the scattering ratio calculation is being performed are affected. For example, the use of 75 cm^{-1} (100 cm^{-1}) width passband implies [1] that the value of $F_N(T)$ ($F_O(T)$) changes between the surface and 8 km by approximately 0.8% (1.7%) assuming a 50K temperature difference. Since $F_N(T)$ and $F_O(T)$ increase with height, the effect on scattering ratios measured in the boundary layer is to decrease the value compared to the traditional technique that does not account for these temperature related changes.

The effect of the additive term, $F_R(T)$, has a relatively small percentage effect on the scattering ratio value, \mathcal{R} . However, the aerosol backscatter coefficient is proportional to $\mathcal{R} - 1$ so that relatively small values of $F_R(T)$ can have a large effect on the backscatter coefficient. The situation is quite similar to that of a High Spectral Resolution Lidar where the rotational Raman lines are excluded [40] from the measurement and a correction must be made for the excluded part of the cross section. Both changes in the value of $F_R(T)$ with height and its absolute value affect the calculation of \mathcal{R} . For example, if a $\sim 25 \text{ cm}^{-1}$ bandpass is used to measure the Rayleigh-Mie signal [1], figure 1 indicates that the value of $F_R(T)$ is ~ 0.97 and nearly height independent. The effect of this on the computation

of the backscatter coefficient is shown in figure 9 where the traditional method of calculating aerosol scattering ratio [9] [13] that neglects both $F_R(T)$ and $F_N(T)$ and that of equation 28 are compared. The case simulated is for a $\sim 100 \text{ cm}^{-1}$ wide Raman nitrogen bandpass and a $\sim 25 \text{ cm}^{-1}$ wide Rayleigh-Mie bandpass. The fractional change in $\beta_{\pi}^{aer}(\lambda_L, \tau) / \beta_{\pi}^{mol}(\lambda_L, \tau)$ calculated using the method presented here versus the traditional method is plotted against the scattering ratio calculated in the traditional manner. It is clear from the figure that the fractional change in the ratio of aerosol and molecular backscatter coefficients increases as scattering ratio decreases. For a scattering ratio of 1.2, where the intensity of aerosol scattering is 20% of molecular scattering, the ratio of the two calculations of the backscatter coefficient is approximately 12% for this choice of bandpasses. This figure implies that previous analysis of narrow spectral band Raman lidar measurements of aerosol backscattering have a positive bias that increases as aerosol loading decreases. The fractional error in backscatter coefficient and extinction to backscatter ratio will essentially be the same.

3.5.2 Calibration using an aerosol-free region of the atmosphere

The determination of the value of aerosol scattering ratio from equation 28 is illustrated in figure 10 using SRL data acquired during the night of August 22, 1998 at Andros Island over a 10-minute period. The use of wide band filters for this measurement implies, as in the case for the water vapor mixing ratio profile considered in section 2.7, that the temperature functions have negligible effect. The quantity $F_N(r)P(\lambda_L, \tau) / P(\lambda_N, \tau) - F_R(r)$ is plotted in solid black. The profile slopes toward smaller values as altitude increases due to the differential transmission of the two lidar wavelengths; 351.1 nm for aerosol and 382.3 nm for nitrogen in this example. Due to the wide spectral filters in use for these XeF excimer laser (351 nm) based measurements [25] [18] both $F_N(r)$ and $F_R(r)$ are approximately equal to 1.0 unlike in the case of a narrow passband system. Multiplying by the differential transmission term $\Delta\tau(\lambda_N, \lambda_L, \tau)$ in equation 28 yields the curve shown using a dashed line. $C_N^*(\lambda_L = 351, \tau)$ can now be determined by normalizing the profile to a value of 1.0 in an aerosol-free value region of the atmosphere. As described above, the region between 6 - 10 km is used for this normalization. The dash-dot curve then is the fully processed aerosol backscattering ratio $\beta_{\pi}^{tot}(\lambda_L, \tau) / \beta_{\pi}^R(\lambda_L, \tau)$ with errors calculated using equation 34. In the profiles, one can see small amounts of aerosol

scattering present near the surface with scattering ratios reaching ~ 1.5 . Cirrus clouds can be seen between 13 - 14 *km* where the values are greater than 2.

From this example, $C_N^*(\lambda_L = 351, r)$ has a value of approximately 0.65 outside of the overlap region. Considering equation 29, this value of $C_N^*(\lambda_L = 351, r)$ implies that the ratio of transmission efficiencies, $\xi(\lambda_N) / \xi(\lambda_L)$, must be on the order of 10^3 . In fact, these data were acquired with an ND3 (transmission $= 10^{-3}$) neutral density filter installed in the elastic channel to allow the signal to be acquired using photon counting electronics. This example illustrates that an absolute calibration of the aerosol scattering ratio would be possible using the equations outlined here and a radiometric determination of the transmission efficiency ratio of the lidar channels. The Rayleigh and Raman nitrogen (or oxygen) cross sections are known to better than 5% accuracy eliminating the largest error source that is present in the similar attempt to calibrate the water vapor mixing ratio. The aerosol backscattering coefficient can now be calculated from the aerosol scattering ratio.

3.6 Aerosol backscattering coefficient

The aerosol backscatter coefficient is easily determined from equation 16.

$$\beta^{aer}(\lambda_L, z) = \beta_{\pi}^{mol}(\lambda_L, z)(\mathcal{R}(\lambda_L, z) - 1) \quad (40)$$

Figure 11 shows the aerosol backscatter coefficient corresponding to the aerosol scattering ratio given in figure 10. The errors plotted are those due to the random error in the aerosol scattering ratio given by equation 34.

In terms of backscatter coefficient, which gives the intensity of light back-scattered per incident photon, the tropospheric aerosols yield higher values than the cirrus cloud. In terms of the aerosol scattering ratio given in figure 10, however, the scattering ratio of the cloud is larger than that for the tropospheric aerosols. So, although the cirrus cloud has a lower probability of backscattering an incident photon than does the tropospheric aerosol layer, the ratio of scattering from the cirrus clouds and from molecules at the height of the cirrus cloud is greater than the corresponding ratio for the tropospheric aerosols.

3.7 Extinction to backscatter ratio

The ratio of aerosol extinction to backscatter is an important optical parameter that can yield information about the physical nature of aerosols. For example, quantification of this ratio is useful in studying the growth of aerosols as a function of relative humidity [12]. Aerosol backscatter data from August 26, 1998 are shown in figure 12. Data acquired at an angle of 10 degrees above the horizon were used from this night to improve the vertical resolution. This entails assuming horizontal homogeneity and mapping the data acquired at an angle into the vertical. This permits retrievals of both extinction and backscattering to lower altitudes than is possible with vertical measurements only.

In general during the CAMEX-3 campaign [23], the top of the marine boundary layer (MBL) was observed to be at ~ 1 km as indicated by a roughly constant water vapor mixing ratio. A signature can be seen in the aerosol data at this altitude which likely indicates the top of the marine boundary layer. Above this, the backscattering due to aerosols increases slightly, which is consistent with a change in aerosol composition. This same signature can be seen in the extinction to backscatter ratio (S_a). This ratio is formed using the data shown in figure 6 of part I and figure 12 here. The result is plotted in figure 13. The error bars plotted for S_a are determined using standard error propagation techniques based on the error equations for extinction and backscattering already presented. The relative decrease in S_a above 1 km is another indication of a change in aerosol type. This could be an indication of different aerosol types that have been transported aloft from a different location as opposed to local aerosols that swelled within the marine boundary layer.

The increase in extinction to backscatter ratio up to an altitude of 1 km, the height of the marine boundary layer, could be an indication of aerosol swelling. This is often seen as height increases inside a well-mixed boundary layer. Aerosols begin to swell when the relative humidity increases above $\sim 70\%$ [41]. Since a well-mixed boundary layer should have a relatively constant mixing ratio and mixing ratio is a conserved quantity, as a parcel of air cools within the boundary layer, the relative humidity of the parcel will increase. Atmospheric temperature typically decreases with altitude, thus the relative humidity is often seen to increase with altitude in the boundary layer. When the relative humidity exceeds $\sim 70\%$, one can expect aerosol swelling to commence if the aerosol has not been previously hydrated

in which case swelling can occur at lower relative humidities. An increase in the aerosol size due to hygroscopic growth increases the forward-scattering more than it increases the backward scattering. In general, the result of this is to increase the particle extinction at the expense of backscattering thus increasing the ratio. Thus, the increase in S_a between 0.5 km and 1.0 km is consistent with aerosol swelling due to increases in relative humidity above the threshold 70% value. In fact, measurements of atmospheric relative humidity made by an Atmospheric Emitted Radiance Interferometer (AERI) [42] at the same time as these lidar measurements indicated that relative humidities exceeded 70% between approximately 0.4 km and 1.1 km supporting the conclusion that the increase in S_a below 1.0 km is due to aerosol growth.

4 Summary and conclusions

As the second of a two-part analysis of the traditional Raman lidar measurements of water vapor and aerosols, the temperature dependent forms of the lidar equations that were developed in part I [1] have been used to derive equations for the water vapor mixing ratio, aerosol scattering ratio, aerosol backscatter coefficient and aerosol extinction to backscatter ratio. The appropriate error equations were also derived for these quantities. The effect of the change of intensity of Raman rotational and vibrational-rotational lines versus temperature were simulated using Gaussian functions for different passband widths. The current ability to accurately model the Rayleigh, Raman water vapor and nitrogen spectra coupled with accurate measurements of lidar system transmission characteristics using a calibration lamp imply that an absolute calibration of both the water vapor and aerosol backscattering measurements is possible. An accurate water vapor calibration will require improved knowledge of the ratio of nitrogen and water vapor cross sections although that may be achievable by careful calibration of the U.S. DOE Raman lidar system. An accurate absolute calibration of aerosol backscattering should be possible now.

It was shown that the use of narrowband detection for the water vapor mixing ratio can change the calculation of water vapor mixing ratio by 5% and more for upper tropospheric measurements while in the case of aerosol scattering ratio the effects can exceed 10% for light aerosol conditions with slightly larger effects found for aerosols confined to

the atmospheric boundary layer. This implies that previous analysis of Raman lidar water vapor and aerosol data may be in error by significant amounts due to these narrow passband effects. This has potential implications for the use of Raman lidar in quantifying upper tropospheric water vapor such as has been done with both the NASA/GSFC SRL and the DOE CART Raman lidar. Measurements of the passband characteristics of these and other narrow passband systems are needed with accuracies of $\sim 0.1 \text{ \AA}$ to apply the temperature corrections developed here with confidence. The influence of temperature dependence of Raman scattering has perhaps a larger effect on the traditional calculations of aerosol backscatter coefficient and extinction to backscatter ratio.

The results developed here indicate that a positive bias will exist in the aerosol backscatter coefficient measured using narrowband detection and that the effect becomes quite large for light aerosol loading. This implies that previous calculations of aerosol scattering properties measured with a narrowband may need to be revised. For a given passband width, this effect increases for smaller values of backscattering. A positive bias in backscattering implies that the extinction to backscatter ratios are correspondingly too low by a similar amount with the effect again increasing as aerosol loading decreases.

The same implications are present in quantifying S_a in thin cirrus clouds. Previous analysis of cirrus cloud S_a based on narrow passband measurements will exhibit a positive bias in the backscatter coefficient that increases as cloud backscatter decreases. This implies that the database of Raman lidar thin cirrus cloud S_a measurements acquired using narrowband detection are increasingly biased toward lower values of S_a as cirrus optical depth decreases.

There is every expectation that Raman lidar will continue to be one of the most powerful remote sensing tools for studying the atmosphere. As the Raman lidar technique moves increasingly into daytime and upper tropospheric measurements, the use of narrowband detection will increase. The results presented here indicate that the basic analytical techniques used to calculate the traditional Raman lidar quantities of water vapor mixing ratio, aerosol scattering ratio, aerosol backscatter coefficient and extinction to backscatter ratio therefore require modification. The temperature dependent functions required for the analysis of data from a particular lidar system may be obtained by contacting the author.

5 Acknowledgements

Support for this activity has come from the NASA Radiation Sciences and Dynamics and Remote Sensing Program as well as the Department of Energy's Atmospheric Radiation Measurements program.

6 References

- [1] D. N. Whiteman, "New examination of the traditional Raman Lidar technique I: temperature dependence and the calculation of atmospheric transmission", *Appl. Opt.*, this issue.
- [2] A. T. Young, "Revised depolarization corrections for atmospheric extinction", *Appl. Opt.*, 19: (20) 3427-3428 (1980).
- [3] A. T. Young, "On the Rayleigh-Scattering Optical Depth of the Atmosphere", *J. Appl. Meteor.*, 20, 328-330 (1980).
- [4] Lord Rayleigh, "On the light from the sky, its polarization and color", *Phil. Mag.*, **41**, 107-120, 274-279 (1871).
- [5] Lord Rayleigh, "On the scattering of light by small particles", *Phil. Mag.*, **41**, 447-454 (1871).
- [6] Born. M. and E. Wolf, *Principles of Optics*, Cambridge University Press, 952 pp. (1999).
- [7] C. F. Bohren and B. A. Albrecht, *Atmospheric Thermodynamics*, Oxford University Press, New York, New York, 402 pp (1998).
- [8] G. Vaughan, D. P. Wareing, L. Thomas, V. Mitev, "Humidity measurements in the free troposphere using Raman backscatter", *Q. J. R. Meteor. Soc.*, **114**, 1471-1484 (1988).
- [9] D. N. Whiteman, S.H. Melfi, and R.A. Ferrare, "Raman lidar system for the measurement of water vapor and aerosols in the earth's atmosphere", *Appl. Opt.*, **31**, No. 16, 3068-3082 (1992).
- [10] U. Wandinger, A. Ansmann, "Experimental determination of the lidar overlap profile with Raman lidar", *Appl. Opt.*, 41 (3): 511-514 (2002)
- [11] M. Bass (Ed.), "Handbook of Optics", McGraw-Hill, Inc., in 2 volumes. (1995).
- [12] R. A. Ferrare, R. A., S. H. Melfi, D. N. Whiteman, K. D. Evans, R. Leifer, "Raman lidar measurements of aerosol extinction and backscattering 1. Methods and comparisons." *J. Geo. Phys. Res.*, **103**, D16, 19663-19672 (1998).
- [13] A. Ansmann, M. Riebesell, C. Weitkamp, E. Voss. W. Lahmann, W. Michaelis, "Combined Raman Elastic-backscatter lidar for vertical profiling of moisture, aerosol extinction, backscatter, and lidar ratio, *Appl. Phys. B.*, 55 (1), 18-28 (1992).

- [14] D. D. Turner, J. E. M. Goldsmith, "Twenty-four-hour Raman lidar water vapor measurements during the Atmospheric radiation Measurement program's 1996 and 1997 water vapor intensive observation periods", *J. Atmos. Ocean. Tech.*, 16: (8) 1062-1076 (1999).
- [15] R. M. Measures, *Laser Remote Sensing Fundamentals and Applications*, (Wiley-Interscience, New York, New York, 1984).
- [16] U. S. Standard Atmosphere. NOAA document S/T 76-1562, National Oceanic and Atmospheric Administration, National Aeronautics and Space Administration, United States Air Force, Washington, DC 227 pp. (1976).
- [17] J. E. M. Goldsmith, F. H. Blair, S. E. Bisson, D. D. Turner, "Turn-key Raman lidar for profiling atmospheric water vapor, clouds, and aerosols", *Appl. Opt.*, 37, 4979-4990 (1998).
- [18] D. N. Whiteman, S. H. Melfi, "Cloud liquid water, mean droplet radius and number density measurements using a Raman lidar", *J. Geophys. Res.*, 104, No. D24, 31411-31419 (1999).
- [19] P. R. Bevington and D. K. Robinson, *Data Reduction and Error Analysis for the Physical Sciences*, McGraw-Hill, 328 pp (1992).
- [20] D. N. Whiteman, G. Schwemmer, T. Berkoff, H. Plotkin, L. Ramos-Izquierdo, G. Pappalardo, "Performance modeling of an airborne Raman water-vapor lidar", *Appl. Opt.*, 40, 3, 375-390. (2001).
- [21] R. A. Ferrare, R.A., S.H. Melfi, D.N. Whiteman, K.D. Evans, F.J. Schmidlin and D.O'C. Starr, "A Comparison of Water Vapor Measurements made by Raman Lidar and Radiosondes", *J. Atmos. Ocean. Tech.*, 12, 1177-1195 (1995).
- [22] Modtran 4 Radiative Transfer Code, The Air Force Research Lab, Space Vehicles Directorate. Hanscom Air Force Base, MA.
- [23] D. N. Whiteman, K. D. Evans, B. Demoz, D. O'C. Starr, D. Tobin, W. Feltz, G. J. Jedlovec, S. I. Gutman, G. K. Schwemmer, M. Cadirola, S. H. Melfi, F. J. Schmidlin, "Raman lidar measurements of water vapor and cirrus clouds during the passage of hurricane Bonnie", *J. Geophys. Res.*, 106, No. D6, 5211-5225 (2001).
- [24] V. Sherlock, A. Hauchecorne, J. Lenoble, "Methodology for the independent calibration of Raman backscatter water-vapor lidar systems", *App. Opt.*, 38, 27, 5816-5837 (1999).
- [25] D. N. Whiteman, W. F. Murphy, N. W. Walsh, K. D. Evans, "Temperature sensitivity of an atmospheric Raman lidar system based on a XeF excimer laser", *Opt. Lett.*, 18, No. 3, 247 - 249 (1993)
- [26] E. R. Miller, J. Wang, and H. L. Cole, "Correction for dry bias in Vaisala radiosonde RH data", *Proceedings of the Ninth ARM Science Team Meeting*, San Antonio, TX, March 22-26, 1999.
- [27] B. M. Lesht, "Reanalysis of radiosonde data from the 1996 and 1997 Water Vapor Intensive Operations Periods: Applications of the Vaisala RS-80H contamination correction algorithm to dual-sonde soundings", *Proceedings of the Ninth ARM Science Team Meeting*, San Antonio, TX, March 22-26, 1999.
- [28] B. M. Lescht, "Uncertainty in radiosonde measurements of temperature and relative humidity estimated from dual-sonde sounds made during the September 1996 ARM Water Vapor IOP". In *Proceedings of the 10th Sympo-*

sium on Meteorological Observations and Instrumentation. Am. Meteorol. Soc., pp. 80-83, Phoenix, AZ, January 11-16, 1998.

- [29] D. N. Whiteman, T. Berkoff, D. D. Turner, T. Tooman, R. Ferrare, L. Heilman, "Research efforts in the absolute calibration of a Raman water vapor lidar", presented at the 20th International Laser Radar Conference, Vichy, France (2000).
- [30] C. M. Penney and M. Lapp, "Raman-scattering cross-section for water vapor", *J. Opt. Soc. Am.*, **66**, 422-425 (1976).
- [31] G. Avila, J. M. Fernandez, B. Mate, G. Tejada, S. Montero, "Ro-vibrational Raman Cross Sections of Water Vapor in the OH Stretching Region", *J. Mol. Spectr.*, **196**, 77-92 (1999).
- [32] G. Herzberg, *Molecular Spectra and Molecular Structure Vol. 1 - Spectra of Diatomic Molecules*, Kreiger Publishing, 660 pp. (1989).
- [33] C. M. Penney, R. L. St. Peters, M. Lapp, "Absolute rotational Raman cross sections for N₂, O₂, CO₂", *J. Opt. Soc. Am.*, **64**, 5, 712-716 (1976).
- [34] W. S. Heaps, J. Burris, J. A. French, "Lidar technique for remote measurement of temperature by use of vibrational-rotational Raman spectroscopy", *Appl. Opt.* **36**: (36) 9402-9405 (1997).
- [35] Personal communication, Dr. Anthony Clough, Atmospheric and Environmental Research, Inc. (2002).
- [36] D. Muller, K. Franke, F. Wagner, D. Althausen, A. Ansmann, J. Heintzenberg, "Vertical profiling of optical and physical particle properties over the tropical Indian Ocean with six-wavelength lidar 1. Seasonal cycle", *J. Geophys. Res. - Atmos.* **106**: (D22) 28567-28575 (2001).
- [37] D. Muller, D., K. Franke, F. Wagner, D. Althausen, A. Ansmann, J. Heintzenberg, G. Verver, "Vertical profiling of optical and physical particle properties over the tropical Indian Ocean with six-wavelength lidar 2. Case studies", *J. Geophys. Res. - Atmos.* **106**: (D22) 28577-28595 (2001).
- [38] P. B. Russell, T. J. Swissler, and M. P. McCormick, "Methodology for error analysis and simulation of lidar measurements", *Appl. Opt.*, **18**, 3783-3797 (1979).
- [39] P. B. Russell, B. M. Morley, J. M. Livingston, G. W. Grams and E. M. Patterson, "Orbiting lidar simulations. 1: Aerosol and cloud measurements by an independent-wavelength technique", *Appl. Opt.*, **21**, 9, 1541-1553 (1982).
- [40] She, C-Y., "Spectral structure of laser light scattering revisited: bandwidths of nonresonant scattering lidars", *Appl. Opt.*, **40**, 27, 4875-4884 (2001).
- [41] A. Deepak and L. H. Ruhnke, *Hygroscopic Aerosols*, (A. Deepak Publishing, 1984).
- [42] W. F. Feltz, W. L. Smith, R. O. Knuteson, H. E. Revercomb, H. M. Woolf, H. B. Howell, "Meteorological applications of temperature and water vapor retrievals from the ground-based Atmospheric Emitted Radiance Interferometer (AERI)", *J. Appl. Meteor.*, **37**: (9) 857-875 (1998).

7 Figure Captions

1. The temperature dependent ratios $F_N(T(r))/F_H(T(r))$ that are needed to evaluate the water vapor mixing ratio are plotted using bandwidths for the water vapor and nitrogen channels that correspond to 0.3 nm and 2.0 nm when excited by 354.7 nm radiation as noted in the legend. For the choice of 0.3 nm bandpass for both water vapor and nitrogen, the temperature dependent ratio decreases by ~4% between the surface and 11 km. Narrower water vapor bandpasses increases the magnitude of this change. The temperature dependent functions F_R, F_N, F_O that are needed for the aerosol scattering ratio calculation are also shown for the same bandpass conditions. For example, a 24 cm^{-1} bandpass for the Rayleigh-Mie signal corresponds to 0.3 nm when excited at 354.7 nm.
2. Five synthesized aerosol extinction profiles to test the influence of various aerosol loadings on the calculation of differential transmission. The aerosol optical depth of the profiles ranges from $\tau = 0$ (pure Rayleigh) to $\tau = 2.0$ (extremely hazy). All profiles equal 0 above 2.0 km.
3. Differential transmission term for the calculation of water vapor mixing ratio when using the XeF excimer (351.1 nm) or Nd:YAG laser (354.7 nm). Various modeled aerosol loadings ranging from a pure Rayleigh atmosphere to extremely hazy ($\tau = 2.0$) are considered. Changes in aerosol optical depth of 0.5 change the differential transmission by approximately 2%.
4. Differential transmission profile for the water vapor mixing ratio calculation using an aerosol optical depth of 1.0 and allowing the Angstrom coefficient to vary between 0.8 and 1.2. The differential transmission term changes by less than 2% over this range of k . The profiles are appropriate for a laser output wavelength of ~350 nm.
5. Comparison of a 10-minute SRL water vapor mixing ratio profile with that of a coincidentally launched radiosonde with a linear scale on the left and a log scale on the right. The SRL water vapor calibration was determined through a best fit procedure between the lidar and the radiosonde between 1 - 3 km. The radiosonde was launched at 0022 or 0.37 UT.
6. Differential transmission profiles required for the aerosol scattering ratio using either Raman nitrogen (left) or oxygen (right) for a range of optical depths. The laser wavelength simulated is 351.1 nm. Increasing the optical depth makes the differential transmission term larger with height. $\tau = 0$ indicates pure molecular scattering while $\tau = 2.0$ would indicate very hazy conditions. The standard atmosphere has been used to calculate the molecular extinction.
7. Differential transmission profiles for the aerosol scattering ratio measurement using either the doubled (~532 nm) or tripled (~355 nm) Nd:YAG. The atmospheric conditions considered are 1) pure Rayleigh, 2) aerosol optical thickness of 1.0 and 3) aerosol optical thickness of 0.67 at 532 nm. This latter case simulates measure-

ments at the two laser wavelengths under similar atmospheric conditions. At the longer wavelength, the relative importance of aerosol loading on the values of differential transmission is clear.

8. The sensitivity of the aerosol scattering ratio differential transmission profile to the wavelength scaling of aerosol extinction is tested here. For an aerosol optical depth of 1.0, the aerosol differential transmission term is plotted for $k = 0.8, 1.0$ and 1.2 . The differential transmission term changes by approximately 4% over this range.
9. The error in calculation of aerosol scattering ratio created by ignoring the temperature dependent functions is explored here when using a $\sim 100 \text{ cm}^{-1}$ wide Raman nitrogen bandpass and a $\sim 25 \text{ cm}^{-1}$ wide Rayleigh-Mie bandpass. The fractional change between the full temperature dependent formulation of the aerosol scattering and the traditional calculation which ignores these effects is plotted against the traditional results. For this choice of bandpass widths, the error in the quantification of the aerosol backscatter coefficient will be $\sim 12\%$ when the traditional scattering ratio calculation yields a value of 1.2. This implies that there is a positive bias to aerosol backscatter determination using narrowband detection if the temperature functions are not accounted for.
10. The steps in the evaluation of equation 28 are shown using data acquired by the SRL over a 10-minute period on the night of August 22, 1998. In solid line is shown the raw ratio of the lidar quantity $F_N(T(r))P(\lambda_L, r)/P(\lambda_N, r) \Delta\tau(\lambda_N, F_R(T(r)))$. The dashed curve is the same quantity after multiplying the first term by the differential transmission profile $\Delta\tau(\lambda_N, \lambda_L, r)$ calculated from equation 28 using actual lidar aerosol extinction data and molecular number density from a radiosonde. Finally the value of C_N^* is determined by normalizing the curve between 6 - 10 km where aerosol scattering is negligible. The final curve is the fully processed aerosol backscattering ratio given by $\beta_\pi^{\text{tot}}(\lambda_L, r)/\beta_\pi^R(\lambda_L, r)$. The random error in the final signal is also shown.
11. Aerosol backscattering coefficient calculated on the night of August 22, 1998. Tropospheric aerosols can be seen up to altitudes of approximately 3 km while a cirrus cloud layer is apparent between 13 and 15 km.
12. Aerosol backscatter coefficient for the tropospheric aerosols that were present during the night of August 26, 1998 at Andros Island. Data acquired at a low elevation angle have been used to improve the measurement of extinction by converting the angle profile to a vertical profile using an assumption of horizontal homogeneity.
13. Aerosol extinction to backscatter ratio using a 20-minute summation of data on the night of August 26, 1998 in Andros Island, Bahamas.

8 Figures

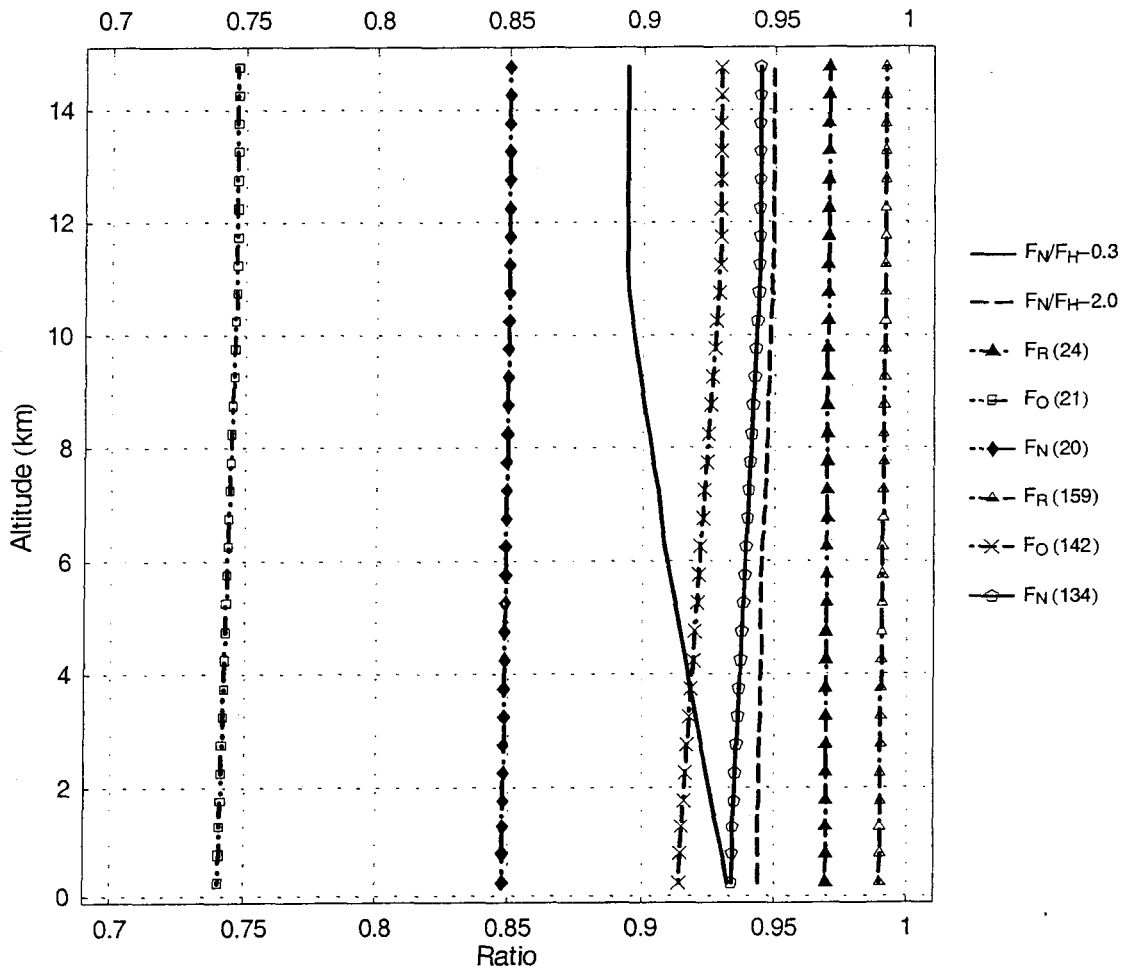


Figure 1:

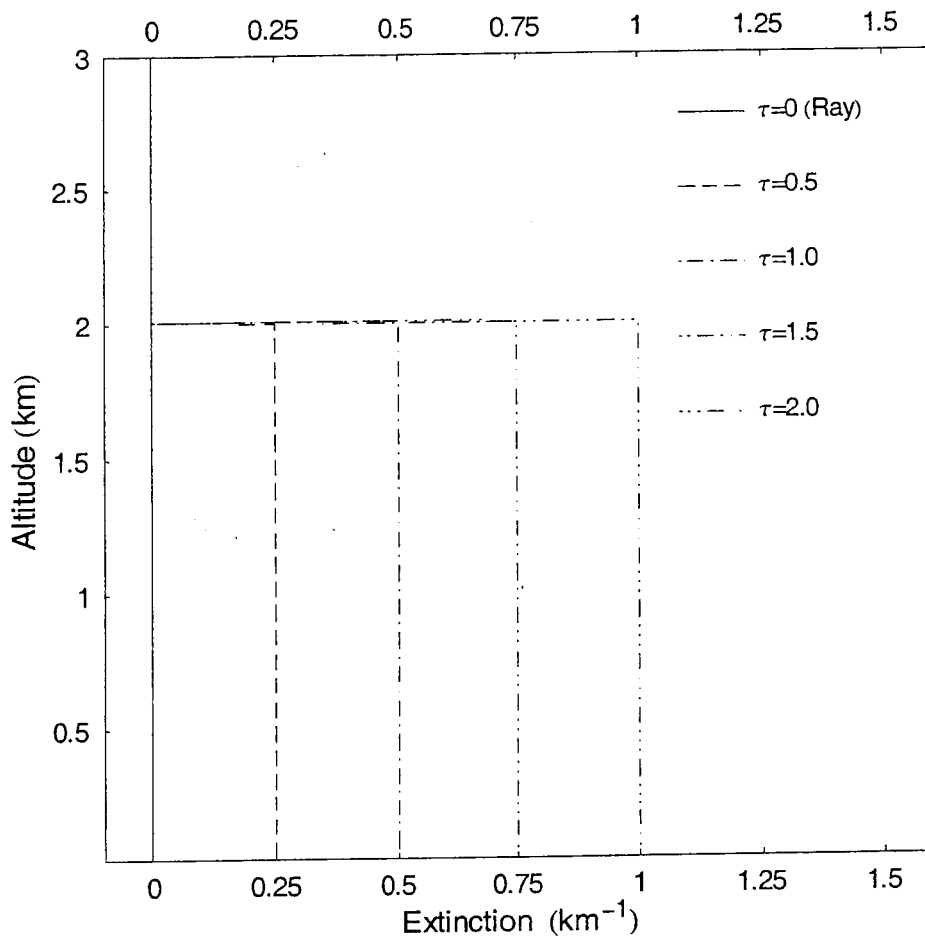


Figure 2:

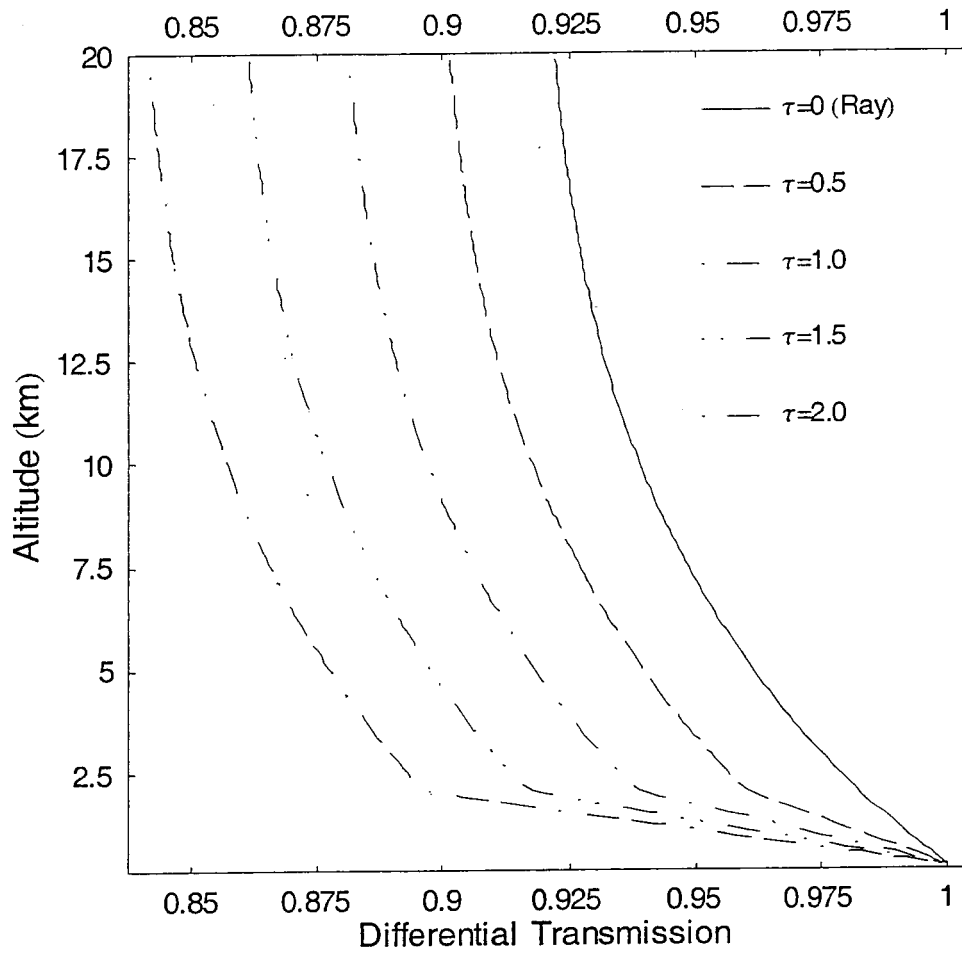


Figure 3:

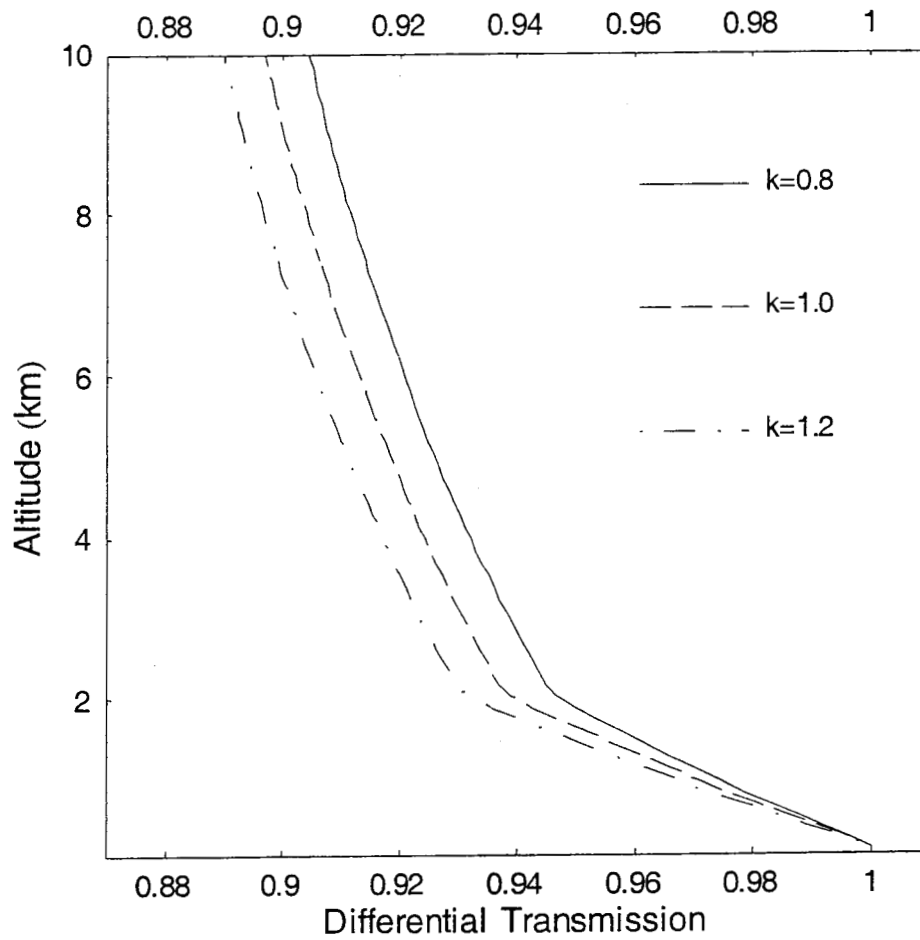


Figure 4:

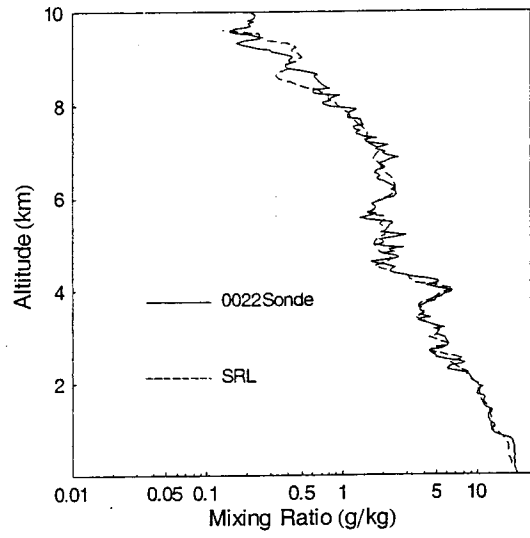
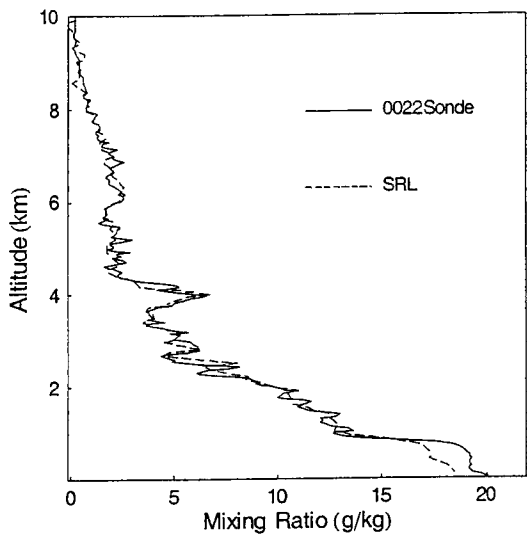


Figure 5:

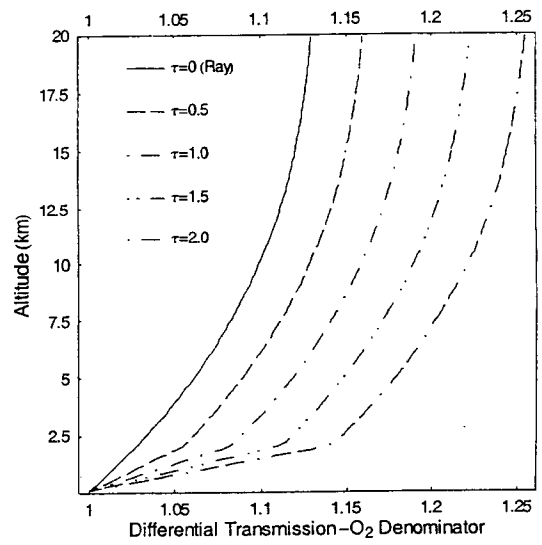
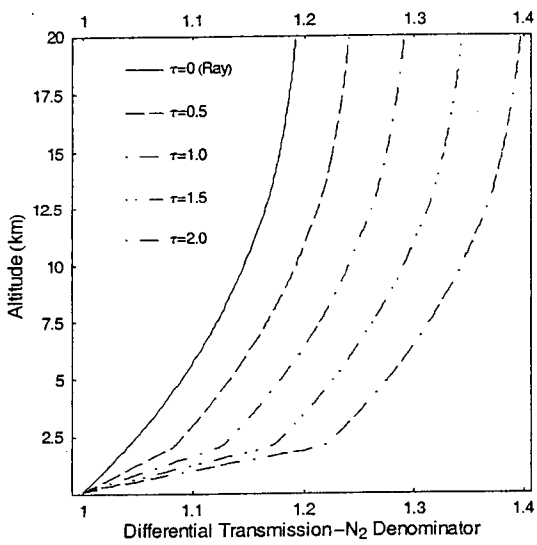


Figure 6:

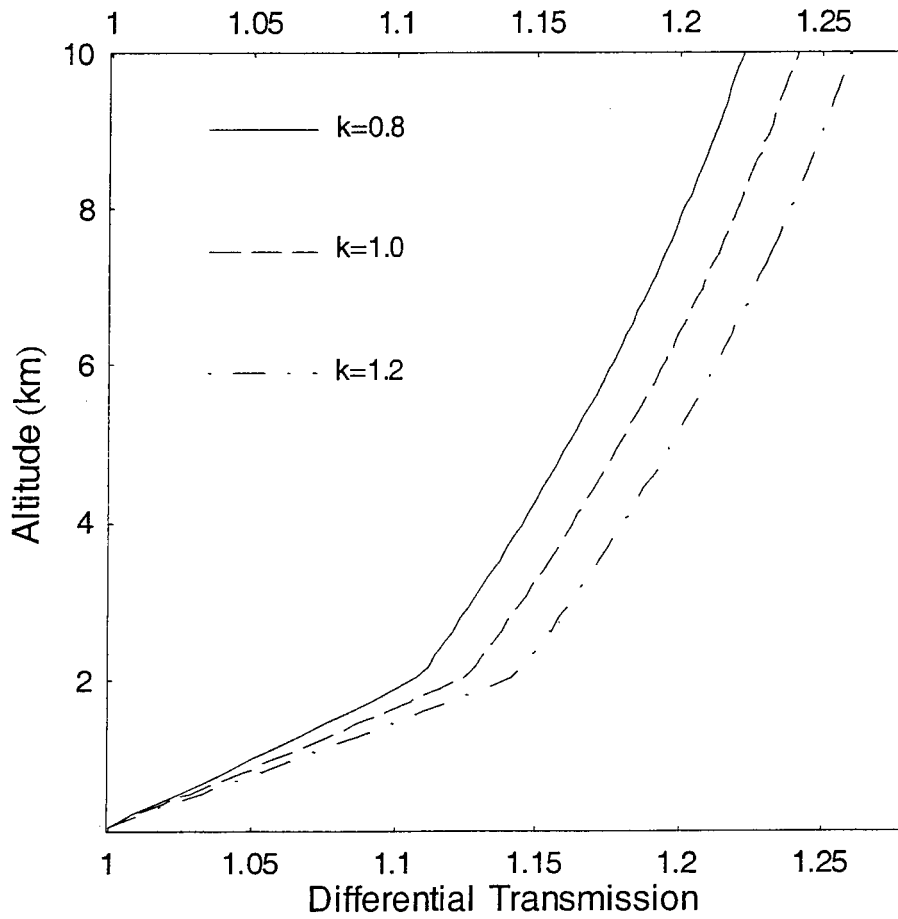


Figure 7:

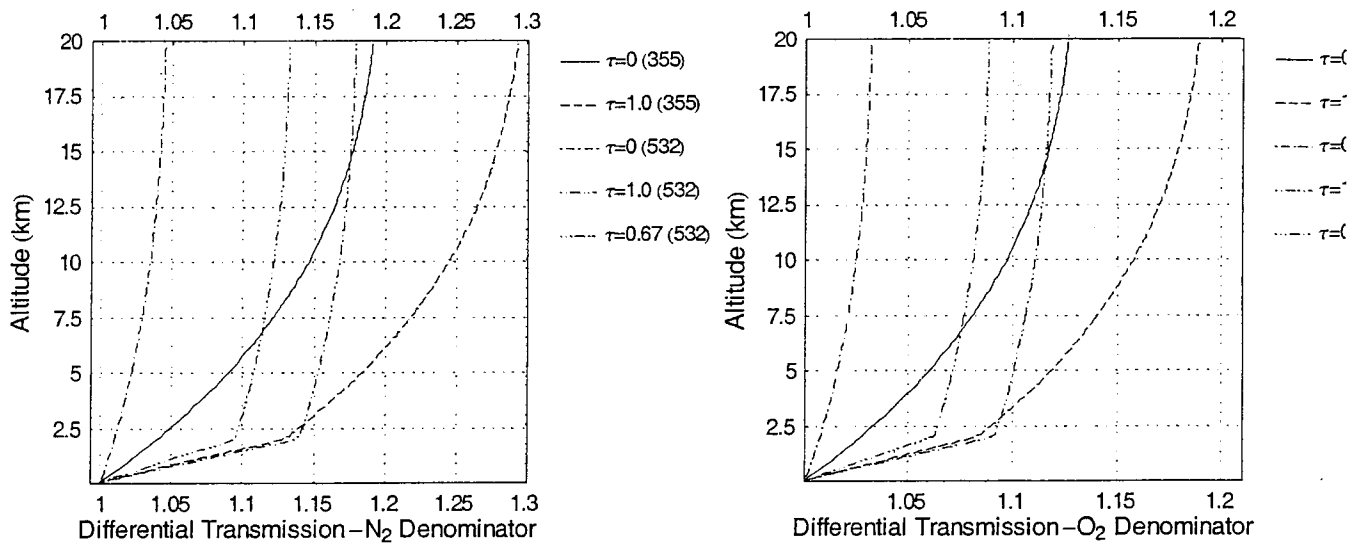


Figure 8:

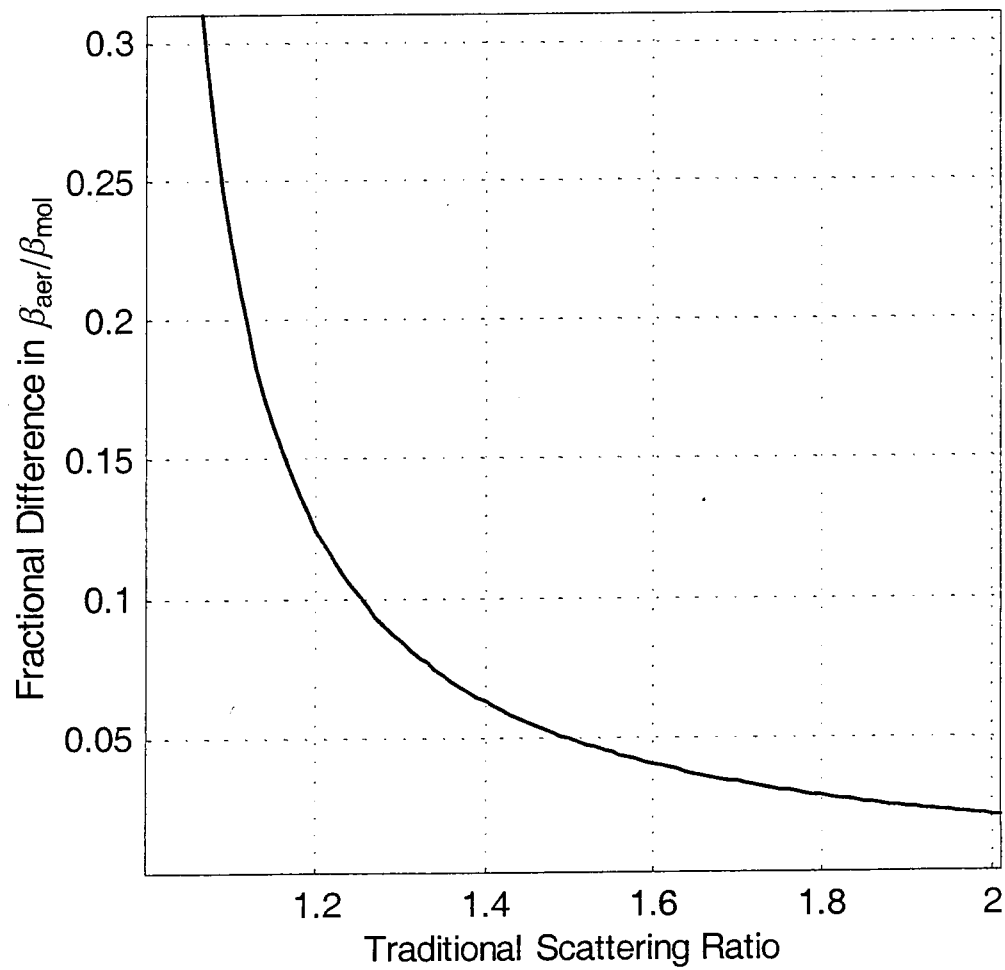


Figure 9:

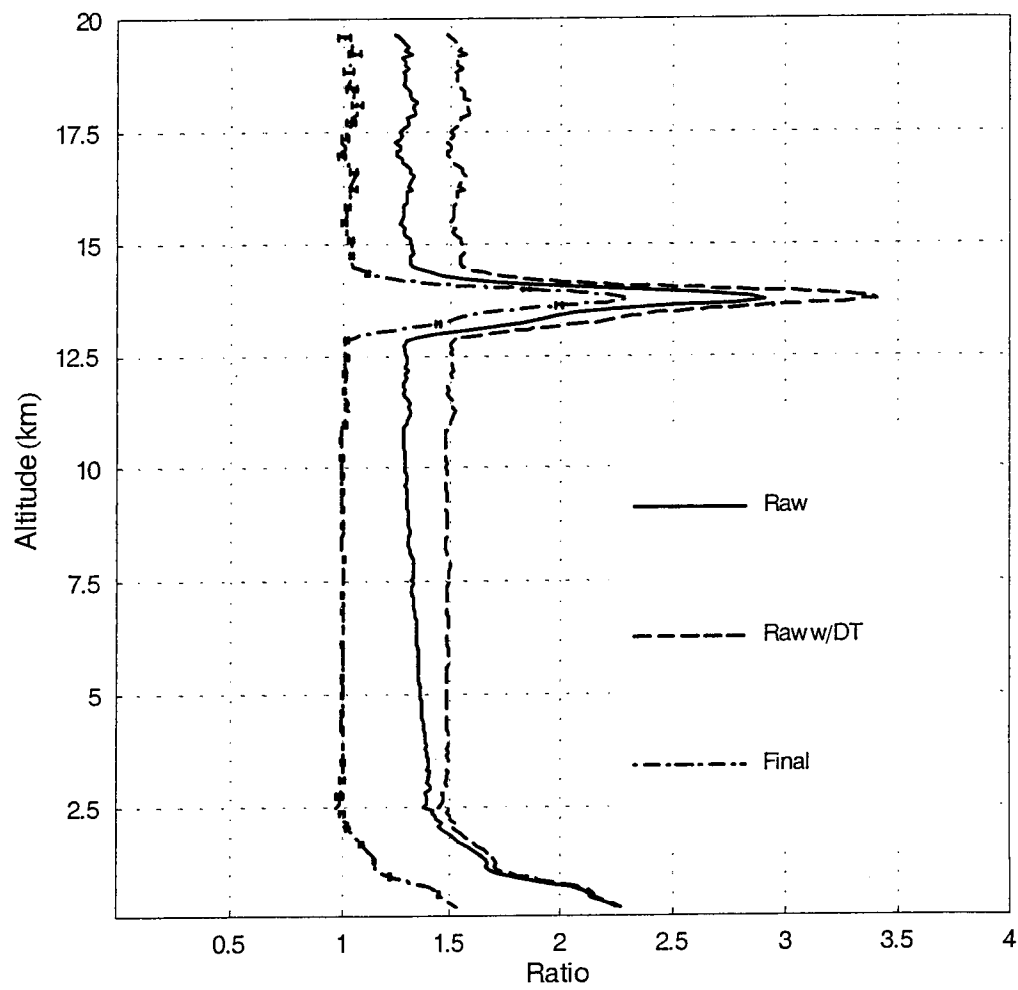


Figure 10:

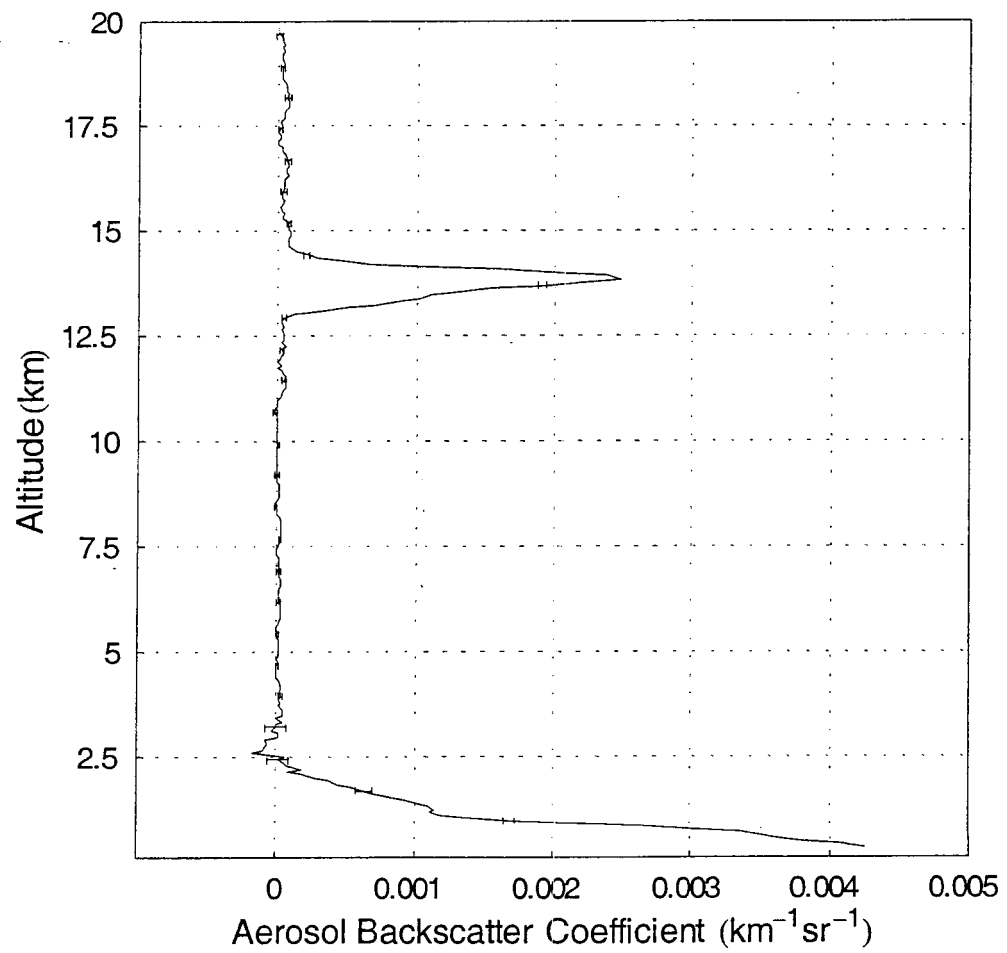


Figure 11:

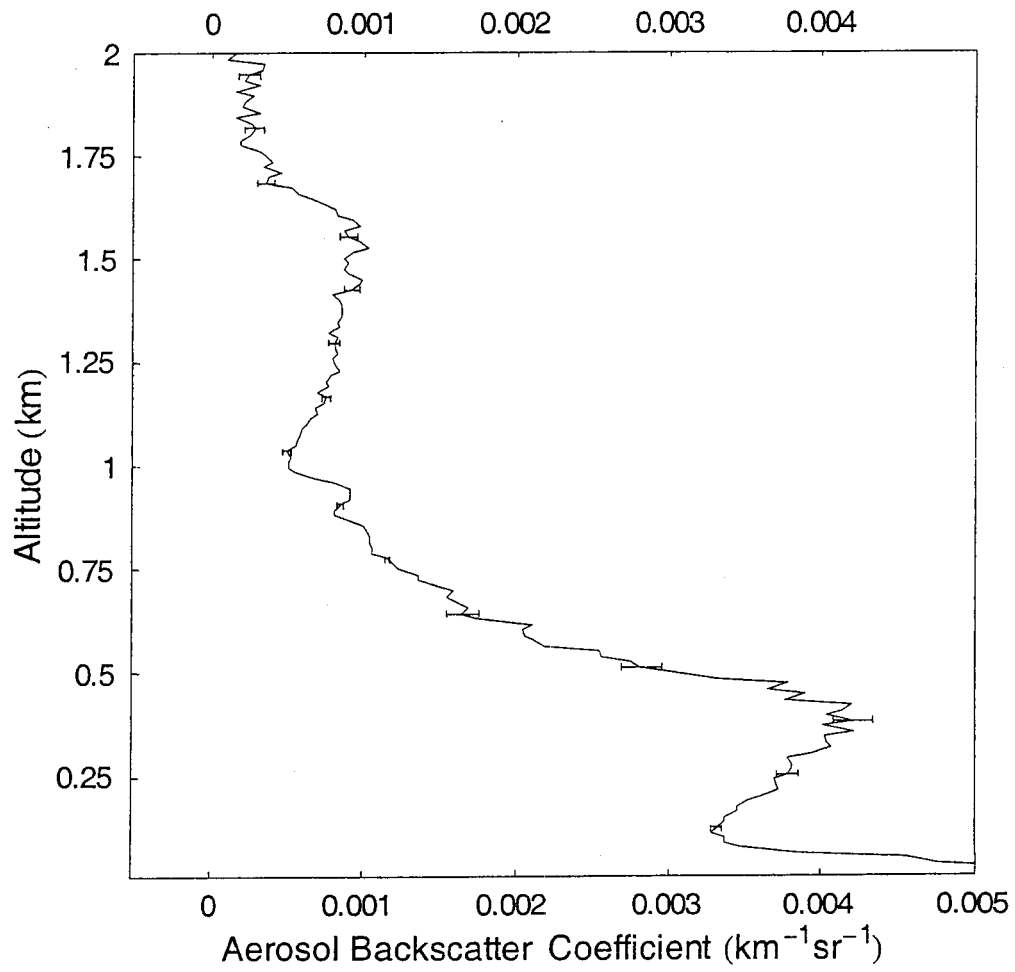


Figure 12:

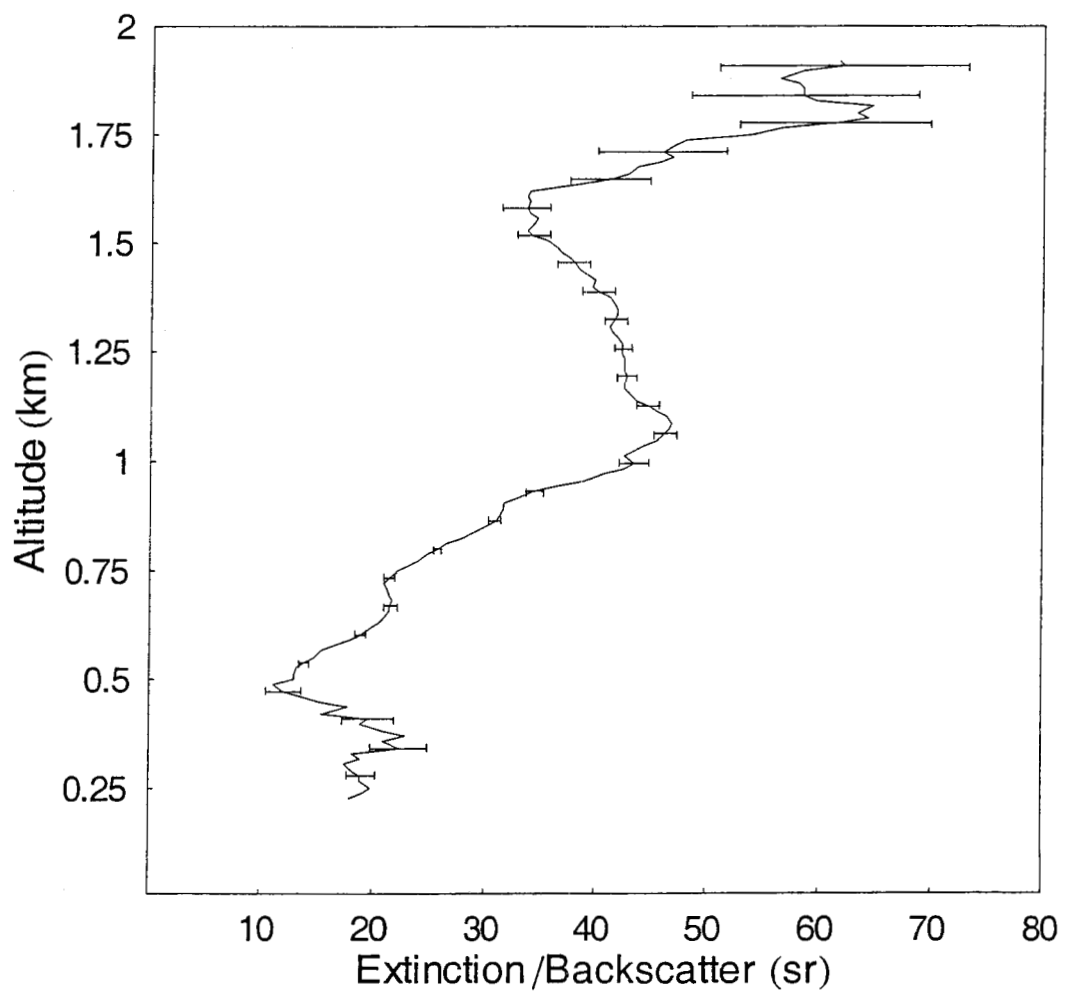


Figure 13: